TÉCNICO LISBOA

CFD and Finite Element Investigation of Water Impact on Composite Panels

Nuno Rodrigo Soares Borges e Silva

Thesis to obtain the Master of Science Degree in

Naval Architecture and Ocean Engineering

Supervisors

Prof. Shan Wang

Examination Committee

Prof. Carlos Guedes Soares

Dr. Gong Xiang

Prof. Shan Wang

16th of December 2019

This page was intentionally left blank

Acknowledgments

First and foremost, I would like to thank Professor Shan Wang and Professor Carlos Guedes Soares, not only, for the opportunity to continue their research on this particular field of study, but also for their unconditional support during the development of this thesis.

I also want to thank my family, especially my parents, for their support, encouragement and for providing me all the means necessary to complete this journey.

A special thanks to Alexandra, for the daily support and motivation, always making sure that I'm focused in my goals.

Finally, I am grateful to my colleagues, for their support and help during these past years during my studies and also for their guidance in my first year at *Instituto Superior Técnico.*

This page was intentionally left blank

Resumo

Atualmente, o uso de materiais compósitos na indústria naval está a tornar-se padrão para certos tipos de navios, torna-se então importante entender o comportamento destes materiais para que possamos aproveitá-los de uma forma segura e eficiente. Nesta dissertação, são abordados os efeitos dos esforços induzidos pelo impacto da água, em estruturas construídas em materiais compósitos, neste caso, numa cunha com estrutura em materiais compósitos. Este problema de interação fluido-estrutura é abordado usando a formulação ALE incluída no software comercial LS-DYNA. O modelo de fluidos computacional apresentado é validado através da comparação dos resultados da estrutura rígida com dados experimentais publicados. O modelo de elementos finitos é também validado através da simulação com dados de entrada fornecidos por outro estudo publicado, comparando os resultados estruturais elásticos obtidos relativos á estrutura em compósitos, com os resultados da mesma pesquisa. É simulado o impacto na água de várias cunhas, combinando vários ângulos e velocidades de entrada. Por fim, os resultados das forças de impacto e deslocamentos nos painéis são então resumidos e discutidos.

Palavras-Chave: Impacto água painel compósito, FSI painel impacto água, formulação ALE

This page was intentionally left blank

Abstract

Nowadays, the use of composite materials in the marine industry is becoming standard for some type of ships, therefore, it's very important to understand its mechanics so we can take advantage of these materials in a safe and efficient way. In this study, the effects of the water impact induced loads, also known as slamming loads, on the water entry of a composite wedge are studied. This fluid-structure interaction problem is investigated using the ALE formulation included in the commercial software LS-DYNA. The computational fluid dynamics model presented is validated through the comparison of the rigid structure results with published experimental data. The finite element model is also validated through the simulation with input data given from another published research and with the comparison of the composite structural results from the same research. The water entries of composite panels with the combination of different deadrise angles and entry velocities are simulated. The results of the slamming loads and displacements on the wedge are then summarized and discussed.

Keywords: Slamming composite plate, FSI plate slamming, ALE formulation

This page was intentionally left blank

Contents

This page was intentionally left blank

List of tables

This page was intentionally left blank

List of figures

This page was intentionally left blank

Nomenclature

Slamming theory nomenclature

β	Deadrise angle
V	Velocity
L	Wetted width
$\emptyset$	Velocity potential
t	Time
p	Pressure
p_0	Atmosferic Pressure
ρ	Fluid density
H	Distance between the keel and the calm water surface
C_p	Non-dimensional pressure coefficient
$C_{p\,max}$	Maximum non-dimensional pressure coefficient
p_{max}	Maximum Pressure
k	Regression non-dimensional coefficient
k_1	Regression polynomial coefficient

Composites nomenclature

m_f	Fibres mass
m_r	Resin mass
M_f	Fibre mass fraction
v_f	Fibres volume
v_r	Resin volume
ρ_f	Fibres density
ρ_r	Resin density
k_1	Regression polynomial coefficient
t_{ply}	Cured ply thickness
E	Elastic modulus
G	Shear modulus
υ	Poisson coefficient

Geometry nomenclature

x	Horizontal coordinate
y	Vertical coordinate
hw	Heigth until full submersion
h	Wedge height
d	Wedge length
w	Wedge width

Miscellaneous

FSI	Fluid Structure Interaction
ALE	Arbitrary Lagrangian and Eulerian
CFD	Computational fluid dynamics
FEM	Finite element method
EOS	Equation of state
FRP	Fiber-reinforced polymer

1. Introduction

1.1 Slamming problem overview

In naval architecture, “slamming” is the term used to describe the impact of the ship bottom in the water at high velocity. The impact loads due to the high pressure build up tend to be higher near the ship’s bow, since the relative velocity between the ship and the water is higher. These loads can be very extreme not only on the bottom of the ship but also in the upper regions of the hull where there is a lot of water displacement and splash up, as can be seen in Figure 1.1. For this reason, engineers generally have to take special attention with the design, taking in account this type of loads which can cause significant local damage to the ship’s structure.

Figure 1.1: Bow of a ship experiencing heavy weather

A lot of studies from different authors have been performed regarding this subject, showing that there are many different factors that can influence this problem. Earlier studies rapidly concluded that the deadrise and the impact velocity are the parameters that contribute the most for this type of loading on the structure. Naturally, the pressure is higher when the velocity is higher and the deadrise is low, as it results in a more violent and sudden impact. Although this may seem logical when considering a simple “V-Bottom” hull, there are other effects that can have a big influence on the loadings when considering more complex geometries, for instance, the formation of air pockets as was numerically investigated by Wang and Guedes Soares [24].

Faltinsen [8] demonstrated that the hydroelasticity, which is the term used to describe the behavior of a structure when subjected to the hydrodynamic loads that are produced due to its own elastic deformation, can also contribute for the stresses induced on the structure, especially when the deadrise is small.

1.2 Composite structures

With the industry opting more for the use of composite materials due to benefits, it's very important that the engineers and ship builders take special care when designing structures with this type of materials, especially in highly loaded applications. The benefits of this type of materials are related to its strength to weight ratio and to its low maintenance, but whatever the reason for using these type materials, one should always keep in mind that these are very sensible materials that may be prone to failure when not design with enough margins or when are not built with enough quality.

Nowadays, the composites are becoming the standard material to build pleasure crafts and even small ferries or workboats, especially if the design requires high speed. It's very important to take special care with the slamming loads that may be induced to these ship's structures has these vessels also have the tendency to be designed with small deadrise angles and to reach high speeds, which as explained earlier, results in very high slamming loads.

Being the composite materials composed by at least two materials, it imposes additional work and difficulty when designing structures with these types of materials. The most common type of composite material used in this industry is the FRP, that is composed by a resin, which is the matrix, and the fibres, which are the reinforcement material. The added difficulty on the design it´s due to the fact that these materials have very different properties and although the resin can be considered isotropic, the fibres are generally orthotropic.

Using CFD software's to accurately calculate the loadings on the structure in conjunction with FEM software's to the actual structural design is one of the fastest, safest and cheaper way of designing composite structures that are subjected to hydrodynamic loads. It's for these reasons that the industry is investing in the computer aid design tools and this is also the motivation behind the development of this work.

1.3 Thesis objectives

The main aim of this study is to investigate the water impact problem on composite sandwich panels. Addressing this type of fluid-structure interaction problem using only analytical methods can be very difficult and time consuming. Regarding the fluid part, the equations are generally very complex to be solved manually and the available theories proposed by previous investigators generally have some limitations in terms of application. On the other hand, the structural part of the problem is generally simpler, but on this case, we are investigating on composite sandwich panels which can also add some complexity.

In this study, the slamming problem is addressed via numerical methods. Using the ALE formulation included in the commercial software LS-DYNA, it is possible to investigate the effect of water impact on composite panels in a more efficient way.

The FSI model implement in LS-DYNA version 971, is validated by comparing the rigid body result obtained from the software with other analytical and experimental results. The composite plate model is

also verified by running the model in the same conditions that an experiment with a composite sandwich plate was performed by Hasson et al. [10].

1.4 Thesis structure

This study is composed by eight chapters, being the first one the present introduction, where the slamming problem is presented, followed by the thesis objectives and structure.

Chapter two is dedicated to the current state-of-art, in which the theoretical background regarding the slamming problem and the composite materials are presented. This will include a brief explanation of the adopted formulations used along this thesis.

The computational model and all its details, including mesh size, element selection and other relevant parameters are presented in chapter three.

In the fourth chapter, the rigid body model validation take place, by comparing the hydrodynamics results of the rigid body wedge with other numerical and experimental results from published simulations.

Chapter five presents the results for the flexible composite body model validation, where simulations are performed in similar conditions than the ones from a published experiment with composite sandwich plate.

In chapter six, a parametric study is carried, where the effects of some of the computational model parameters, for instance the mesh size, are investigated.

In the seventh chapter, the full hydroelasticity study is carried. The effects of different impacts velocities and deadrise angles are investigated, along with the hydroelasticity effect.

The eighth and final chapter, is the one where this thesis conclusions are presented.

This page was intentionally left blank

2. State of the art

The slamming problem has been in investigation for a long time. Earlier the problem was approached using analytical or experimental methodology. It resulted in a considerable amount of different formulations and theories, but with the more recent developments in numerical methods, the tendency is to research this kind of problems using numerical approaches. Although these computational methods are generally offering good results, there is still margin for improvement and fine tuning, so the numerical results become more accurate and reliable.

In this chapter, a brief review will be made, regarding the formulations and theories that were published up until today. These will be useful in the next chapters for comparing results.

2.1 Historical background

In terms of the analytical approach, the first important contribute to this subject was given by von Kármàn [21]. While trying to develop a simpler way to calculate the pressure forces acting on seaplane floater during landing, he was able to develop an analytical formulation that can be applied to a two-dimensional wedge impacting the water surface. It was proven that von Kármàn [21] theory could be used as a good approximation when dealing with medium to high deadrise angle wedges, but the theory didn´t considered important hydrodynamic effects like the water rise along the wedge, which can be very important, especially at low deadrise angles.

Later, Wagner [22] generalized von Kármàn´s work and developed a formulation that could take in account the water splash-up not considered by the former. Since then, much work has been performed and other formulations have also risen but many of them are still based on the Wagner´s theory. Those are theories like Armand J.L. and Cointe [4], which were also pioneers by presenting a formulation which took in consideration the effect of the nonlinear jet flow. Another important formulation based on Wagner´s is the one presented by Zhao and Faltinsen [26], this time, with a numerical approach to the problem that would enable the study of two-dimensional bodies with arbitrary cross-sections.

The research continued by Zhao et al. [27] with the addition of a flow separation module to the numerical formulation developed earlier. Their research also included experimental tests carried at MARINTEK, that verified the theory. This also motivated investigators, like Mei et al. [14], to extend the research on this subject and to apply the slamming problem to other geometries like a bow-flared section.

On the experimental side, some research was done by Ochi and Motter [15], Stavovy and Chuang [18], in which they present different series of polynomials that approximate their results from the experiments.

Currently, the problem has been addressed mainly by numerical methods, as computational power is becoming powerful. Stenius et al. [19] and Aquelet et al. [3] opted for the numerical approach and started by studying the influence of the numerical model parameters, like the mesh size, on the final slamming results. Alexandru et al. [1] also carried and important numerical study. By simulating the same

slamming problem with different commercial numerical codes, they found that, although results were generally similar, there are some cases where the results can differ. Wang and Guedes Soares [23] also compared their numerical results obtained from LS-DYNA with the different analytical theories and experiments discussed above, having concluded that the results agreed well.

These last studies were mainly applied to rigid wedges or other cross sections. Lately, some investigators have been studying the effects of hydroelasticity applied to the slamming problem, like Lu et al. [12] and Stenius et al. [20]. Wang and Guedes Soares [25] also continued their previous research, now considering the hydroelasticity.

Regarding the slamming problem applied to composite wedges, several research studies have been performed lately, mainly with numerical approaches but also with experiments. Qin and Batra [16] started by developing a hydroelasticity model for sandwich composite panels applying it with the Wagner´s impact theory. This formulation was later upgraded by Ray and Batra [17], now including a failure module. Kaushik and Batra [11] also performed an extensive investigation on the subject, using the ALE formulation provided by LS-DYNA and accessing important aspects like the composite delamination.

Several investigators have been conduction experiments related to the subject with composites materials. Beginning with Allen and Battley [2] who did extensive testing using different laminates. By experimenting laminates with different stiffnesses, it enabled the investigators to have a better understanding on the effects of the hydroelasticity. Hasson et al. [9] [10] also did experimental work on composites, firstly with monolithic plates and then with sandwich plates.

2.2 Slamming theory

2.2.1 Wagner´s theory

Being the Wagner [22] theory the base for many other slamming formulations it´s important to make a brief resume of the analytical approach:

Wagner´s [22] formulation is based in three assumptions:

-The fluid is inviscid and incompressible;

-The fluid accelaration is much larger than the gravity accelaration;

-The wedge draft during the water entry is much smaller than the wetted width.

These assumptions simplify the problem and alow the application of the Bernoulli equation.

Figure 2.1 displays, the theory sketch, in which V is the velocity, β the deadrise angle and L the wetted width:

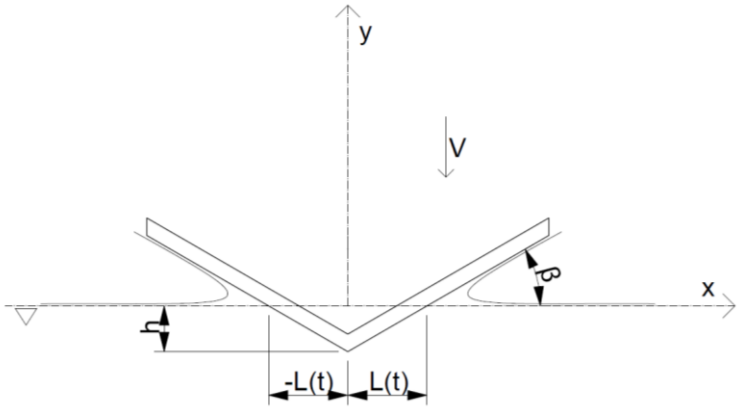

Figure 2.1: Wagner´s theory sketch.

Wagner [22] expressed the velocity potential on the body surface can be expressed as:

$$\emptyset = -V\sqrt{L^2 - x^2}, |x| \leq L(t) \tag{2.1}$$

The pressure distribution can be obtained by Bernoulli equation:

$$\frac{p - p_0}{\rho} = -\frac{d\emptyset}{dt} - \frac{1}{2}\left(\left(\frac{d\emptyset}{dx}\right)^2 + \left(\frac{d\emptyset}{dy}\right)^2\right) \tag{2.2}$$

Taking in account the velocity potential (2.1), and neglecting the effect of the gravity results in:

$$\frac{p - p_0}{\rho} = V\frac{L}{\sqrt{L^2 - x^2}}\frac{dL}{dt} + \sqrt{L^2 - x^2}\frac{dV}{dt} - \frac{V^2}{2}\frac{x^2}{L^2 - x^2} \tag{2.3}$$

The vertical distance between the wedge keel and the calm water surface is given by:

$$H(t) = \int_0^t V(t)\, dt \tag{2.4}$$

Then, the wetted width is given by:

$$L(t) = \frac{\pi}{2\tan\beta}\int_0^t V(t)\, dt \tag{2.5}$$

Assuming that the drop velocity is constant, it results in:

$$\frac{dL}{dt} = \frac{\pi}{2\tan\beta}V \tag{2.6}$$

The pressure coefficient is given by:

$$C_p = \frac{p - p_0}{\frac{1}{2}\rho V^2} \tag{2.7}$$

Once again, assuming the constant velocity case, the velocity derivative in equation (2.3) is equal to zero. By substituting the equation (2.6) and (2.7) in equation (2.3) it´s obtained:

$$C_p = \frac{\pi}{\tan\beta}\frac{L}{\sqrt{\mathrm{L}^2 - x^2}} - \frac{x^2}{\mathrm{L}^2 - \mathrm{x}^2} \tag{2.8}$$

Which, when resolved to its maximum value results in:

$$C_{p\,max} = 1 + \frac{\pi^2}{4\tan^2\beta} \tag{2.9}$$

2.2.2 Empirical formulations

The slamming pressure is approximated as proportional to the square of the impact velocity:

$$p_{max}(x) = \frac{1}{2}\rho k \left|\frac{dV(x,t)}{dt}\right|^2 \tag{2.10}$$

where k is the non-dimensional proportional constant.

Ochi and Motter [15] research propose a regression equation to model the proportional constant k any ship section:

$$k = \exp\left(1.377 + 2.419a_1 - 0.873a_3 + 9.624a_5\right) \tag{2.11}$$

where $a_1,\ a_3, a_5$ are the regression coefficients, that model the section.

Later, Stavovy and Chuang [18] also presented an empirical formulation for the non-dimensional coefficient:

$$k = \frac{288k_1}{\cos^4\beta(x,t)} \tag{2.12}$$

Where $\beta(x,t)$ is the local impact deadrise and k_1 is a coefficient that can be obtained from the following polynomials:

$$k_1 = \begin{cases} \dfrac{0.37\beta}{2.2} + 0.5 & ,0 \le \beta < 2.2º \\ 2.1820894 - 0.9451815\beta + 0.203754\beta^2 - 0.0233896\beta^3 & \\ +0.0013578\beta^4 - 0.00003132\beta^5 & ,2.2º \le \beta < 11º \\ 4.748742 - 1.3450284\beta + 0.1576516\beta^2 - 0.0092976\beta^3 & \\ +\,0.0002735\beta^4 - 0.00000319864\beta^5 & ,11º \le \beta < 20º \\ (1 + 2.4674/\tan^4\beta)0.76856471/288 & ,20º \le \beta \end{cases} \tag{2.13}$$

2.3 Composite material theory

2.3.1 General overview

As explained earlier, composites are a type of material which combines two or more materials in order to obtain a final material that retains good properties from its constituents. The FRP is one of the most common composite materials and is constituted by the matrix and the reinforcement.

The matrix is a chemical resin, generally made from polyester, vinylester or epoxy, each of them with its own properties and associated benefits. This is the material that will bond to the reinforcement while keeping the part shape, during the curing process.

The reinforcement is a fabric which can be produced in several formats from materials like glass, carbon or even Kevlar. Once again, each one of these materials is used in different applications due to its different properties, for instance, parts made from carbon fibres are very stiff and strong due to the carbon high modulus and strength. On the other hand, the glass fibres are less stiff but will provide high impact resistance due to its flexibility.

The differences between each type of fabric is due to the quantity of fibres in a certain direction and in the way these fibres are kept together. For instance, an unidirectional fabric (0º) only has fibres orientated along the length of the roll of fabric, which means that 100% of the fibres are orientated at 0º. A biaxial fabric can have half its fibres orientated at 0º and the other half at 90º or it can be 45º/-45º.

An FRP part is generally produced by laminating various ply´s of reinforcements. Each reinforcement can be different one to another or can also have different orientations. The most common production method for FRP parts is the wet layup, which basically consists in laying the fibres and impregnating them with the resin, one ply at a time. While it's difficult to produce an assembly of fibre reinforced composite parts without using the wet-layup classic approach, all the industries are starting to opt for other, more advanced, techniques like the infusion or the prepreg, which are beneficial when considering the part quality and weight.

2.3.2 Sandwich construction

The sandwich construction is another type of FRP application, in which, instead of building a solid laminate, a lighter material is used to quickly build thickness with small weight increment. As displayed in the Figure 2.2, the laminate will be composed of two FRP skins with a core material in the middle, usually a foam or a honeycomb.

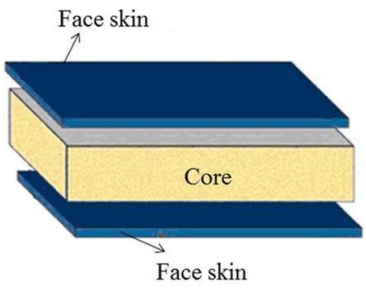

Figure 2.2: Sandwich construction. [7]

As the core material is much lighter than the skins, its thickness can be very high when compared with the skins. This will result in a very stiff and light composite.

Since the skins are situated at the outer part of the laminate and are much stronger and stiffer than the core material, all the tensile and compressive loads are absorbed by them. Then, the core material will only be subjected to shear stresses induced from the skins.

When designing composite structures using the sandwich approach, a good compromise between the core selection and the skins laminate schedule should be found, since both play an important role on the final structure stiffness and strength.

2.3.3 FRP material properties

When designing parts made from FRP composite materials, one off the major difficulties is the determination of the laminate mechanical properties since these are dependent not only on the fiber and matrix but also on the production method and even the facilities and technicians involved in the production.

One of the most important factors that influences the final composite properties is the ratio between the fibres and the resin. This ratio can be expressed in terms of weight or volume and can be presented in relation to the resin or to the fibre.

The following expressions show the relations between the ratios, the volumes and the masses in the composite, where m, v, ρ is the mass, volume and density, respectively, M is the mass fraction and V is the volume fraction. The f, r index will indicate whether the its related to the fibre or to the resin:

$$M_f = \frac{m_f}{m_f + m_r} \tag{2.14}$$

$$V_f = \frac{v_f}{v_f + v_r} \tag{2.15}$$

The general expressions for the density appear as:

$$\rho_f = \frac{m_f}{v_f} \tag{2.16}$$

$$\rho_r = \frac{m_r}{v_r} \tag{2.17}$$

As we are dealing with ratios:

$$V_f = 1 - V_r \tag{2.18}$$

$$M_f = 1 - M_r \tag{2.19}$$

Substituting the last expressions in the first ones it's possible to relate both:

$$M_f = \frac{\rho_f V_f}{\rho_r + V_f(\rho_f - \rho_r \rho_f)} \tag{2.20}$$

$$V_f = \frac{1}{1 + \frac{\rho_f}{\rho_r}\left(\frac{1}{M_f} - 1\right)} \tag{2.21}$$

When working with composite materials, the thickness, in mm, of one cured ply can be approximated by:

$$t_{ply} = \frac{m_f}{1000 \rho_f V_f} \tag{2.22}$$

Relating the thickness with the fiber mass fraction its obtained:

$$t_{ply} = \frac{m_f \left(\frac{1}{\rho_f} + \frac{1 - M_f}{M_f \rho_r}\right)}{1000} \tag{2.23}$$

Generally, it becomes easier to use the fiber mass fraction instead of the fiber volume fraction, as it can be easily calculated by the expression (2.14). In a real production facility, one can easily get the weight of the fibres before the lamination takes place. After the lamination, and with a help of a weight scale, the total laminate weight is known. With these values the fibre mass fraction can easily be calculated.

Bureau Veritas provides a document [5], containing the rules for the structural design of ships built in composites. The rules also propose several tables and empirical formulations for the calculation of FRP mechanical properties.

These rules provide input parameters that can be used to obtain properties for carbon or glass laminates using different polymer resins as the matrix. The results are presented for several types of fabrics like unidirectional fabrics or multi-axial fabrics at 0/90 degrees. It's also possible to obtain the properties for these fabrics when they orientated in other directions through a conversion formulation.

In order to calculate the laminate mechanical properties, it´s necessary to know its constituent´s properties. Regarding the matrix, Bureau Veritas [5] propose the following properties for the most used resins in the industry:

Table 2.1: Resins mechanical properties [5].

	Polyester	***Vinylester***	***Epoxy***	
Density, ρ_r	1200	1100	1250	kg/m^3
Poisson Coefficient, υ_r	0.38	0.26	0.39	-
Elastic Modulus, E_r	3550	3350	3100	MPa
Breaking Strength, σ_r	55	75	75	MPa
Shear Modulus, G_r	1350	1400	1500	MPa
Shear Breaking Strength, τb_r	50	65	80	MPa

As for the most common fibres type, the rules propose the following mechanical properties, either in the fibres direction (0º) or transversely to the fibres (90º):

Table 2.2: Fibres mechanical properties [5].

	E Glass	***R Glass***	***HS Carbon***	***IM Carbon***	***HM Carbon***	***Aramid***	
Density, ρ_f	2570	2520	1790	1750	1880	1450	kg/m^3
Poisson Coefficient at 0º, $\upsilon_{f0º}$	0.238	0.2	0.3	0.32	0.35	0.38	-
Elastic Modulus at 0º, $E_{f0º}$	73100	86000	238000	350000	410000	129000	MPa
Breaking Strength at 0º, $\sigma_{f0º}$	2750	3450	3600	4500	4700	2850	MPa
Poisson Coefficient at 90º, $\upsilon_{f90º}$	0.238	0.2	0.02	0.01	0.01	0.015	-
Elastic Modulus at 90º, $E_{f90º}$	73100	86000	15000	10000	13800	5400	MPa
Breaking Strength at 90º, $\sigma_{f90º}$	170	2000	135	70	60	40	MPa
Shear Modulus, G_f	30000	34600	50000	35000	27000	12000	MPa
Shear Breaking Strength, τ_f	1700	1950	1200	1100	1000	500	MPa

The next set of equations used to calculate the mechanical properties are the ones presented by Bureau Veritas [5] and these are based on the “Rule of mixtures” which is very well-known composite material theory.

The theory was firstly formulated based on unidirectional ply, as the one presented in Figure 2.3, and assuming the following:

-Fibres mechanical properties are uniform;

-Fibres geometry is uniform in the whole fabric;

-Fibres are continuous along the whole fabric;

-Fibres are parallel between each other;

-Bonding between fibres and matrix is perfect (meaning that there is no slippage);

-Poisson effects are negligible

-Strain distribution observed during loadings is uniform in the whole ply.

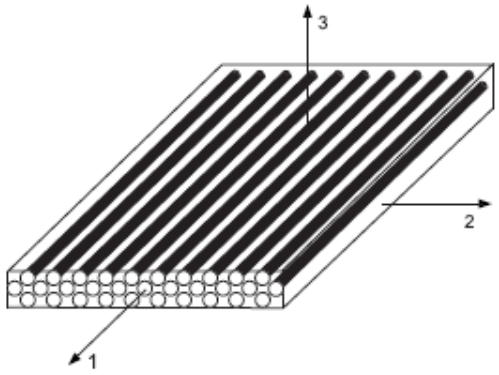

Figure 2.3: Unidirectional ply with a coordinate system representation. [5]

In addition, the organization also propose some additional coefficients which were determined based on their empirical and experimental knowledge. The unidirectional ply elastic modulus equations are given by:

$$E_{UD1} = C_{UD1}\left[E_{f0º}V_f + E_r V_r\right] \tag{2.24}$$

$$E_{UD2} = E_{UD3} = C_{UD2}\left[\frac{\frac{E_f E_r}{1-\upsilon_r{}^2}}{\frac{E_r V_f}{1-\upsilon_r{}^2} + E_f V_r}\right] \tag{2.25}$$

Regarding the shear modulus equations, the theory proposes:

$$G_{UD12} = G_{UD13} = C_{UD12}\left[G_r \frac{1+\eta V_f}{1-\eta V_f}\right] \tag{2.26}$$

$$G_{UD23} = 0.7\, G_{UD12} \tag{2.27}$$

where:

$$\eta = \frac{\frac{G_f}{G_r} - 1}{\frac{G_f}{G_r} + 1} \tag{2.28}$$

Finally, the Poisson coefficients can also be calculated from the same theory:

$$\upsilon_{UD12} = \upsilon_{UD13} = C_{UD\upsilon}\left[\upsilon_f V_f + \upsilon_r V_r\right] \tag{2.29}$$

$$\upsilon_{UD21} = \upsilon_{UD31} = \upsilon_{UD12}\frac{E_{UD2}}{E_{UD1}} \tag{2.30}$$

$$\upsilon_{UD23} = \upsilon_{UD32} = C_{UD\upsilon}\left[\upsilon_f V_f \frac{E_{f90º}}{E_{f0º}} + \upsilon_r V_r\right] \tag{2.31}$$

The coefficients C_{UD1}, C_{UD2}, C_{UD12} and $C_{UD\upsilon}$ are the ones proposed by Bureau Veritas [5]. The rules propose these coefficients based on the fabric type being used on the composite, as demonstrated in Table 2.3:

Table 2.3: Mechanical properties additional coefficients. [5]

	E Glass	***R Glass***	***HS Carbon***	***IM Carbon***	***HM Carbon***	***Aramid***
C_{UD1}	1.00	0.90	1.00	0.85	0.90	0.95
C_{UD2}	0.80	1.20	0.70	0.80	0.85	0.90
C_{UD12}	0.90	1.20	0.90	0.90	1.00	0.55
$C_{UD\upsilon}$	0.90	0.90	0.80	0.75	0.70	0.90

Having described the “Rule of mixtures” theory applied to unidirectional ply’s, it´s possible to extend the theory to other fabric types like the common woven roving which is a 0º/90º fabric. Assuming that this

type of ply is composed by a non-crimped fabric with one unidirectional layer at 0º and one at 90º, the rules [5] propose the following set of equations for the mechanical properties, in which C_{EQ} is the mass ratio of fabric at 0º to the total fabric mass. Q_{ij} and A_{ij} are the coefficients that model the interface between both ply´s and i, j are the indexes indicating the direction:

$$E_{WR1} = \frac{1}{t_{ply}}\left(A_{11} - \frac{{A_{12}}^2}{A_{22}}\right) \tag{2.40}$$

$$E_{WR2} = \frac{1}{t_{ply}}\left(A_{22} - \frac{{A_{12}}^2}{A_{11}}\right) \tag{2.41}$$

$$E_{WR2} = E_{UD23} \tag{2.42}$$

$$G_{WR12} = \frac{1}{t_{ply}} A_{33} \tag{2.43}$$

$$G_{WR13} = G_{WR23} = 0.9\, G_{WR12} \tag{2.44}$$

$$\upsilon_{WR12} = \frac{A_{12}}{A_{22}} \tag{2.45}$$

$$\upsilon_{WR21} = \upsilon_{WR12} = \upsilon_{WR12}\frac{E_{WR2}}{E_{WR1}} \tag{2.46}$$

$$\upsilon_{WR32} = \upsilon_{WR31} = \frac{\upsilon_{UD32} + \upsilon_{UD31}}{2} \tag{2.47}$$

$$\upsilon_{WR13} = \frac{\upsilon_{UD23} + \upsilon_{UD13}}{2} \tag{2.48}$$

where:

$$Q_{11} = \frac{E_{UD1}}{1 - \upsilon_{UD12}\,\upsilon_{UD21}} \tag{2.32}$$

$$Q_{22} = \frac{E_{UD2}}{1 - \upsilon_{UD12}\,\upsilon_{UD21}} \tag{2.33}$$

$$Q_{33} = G_{UD12} \tag{2.34}$$

$$Q_{22} = \frac{E_{UD2}}{1 - \upsilon_{UD12}\,\mathrm{v}_{UD21}} \tag{2.35}$$

$$A_{11} = t_{ply}\left[C_{EQ}Q_{11} + (1 - C_{EQ})Q_{22}\right] \tag{2.36}$$

$$A_{22} = t_{ply}\left[C_{EQ}Q_{22} + (1 - C_{EQ})Q_{11}\right] \tag{2.37}$$

$$A_{33} = t_{ply}Q_{33} \tag{2.38}$$

$$A_{12} = t_{ply}Q_{12} \tag{2.39}$$

3. Computational model

In this study, it was decided to implement the problem on LS-Dyna which is an explicit finite element commercial code that is specialized in solving fluid-structure interaction problems. The ALE formulation is an algorithm which can model the fluid and the structure in a fully coupled way.

In this chapter, the ALE method is briefly explained based on the work of Cheng and Chao [6] and Aquelet et al. [3]. Afterwards, all the details regarding the model are presented, like the element selection, materials, mesh size and boundary conditions.

3.1 ALE formulation

The Arbitrary Lagrangian and Eulerian formulation is a numerical method which consists in using two meshes, one Eulerian mesh for the fluid modelling and one Lagrangian mesh for the structure, to solve fluid structure interaction problems. The algorithm in this formulation is described by the following flowchart:

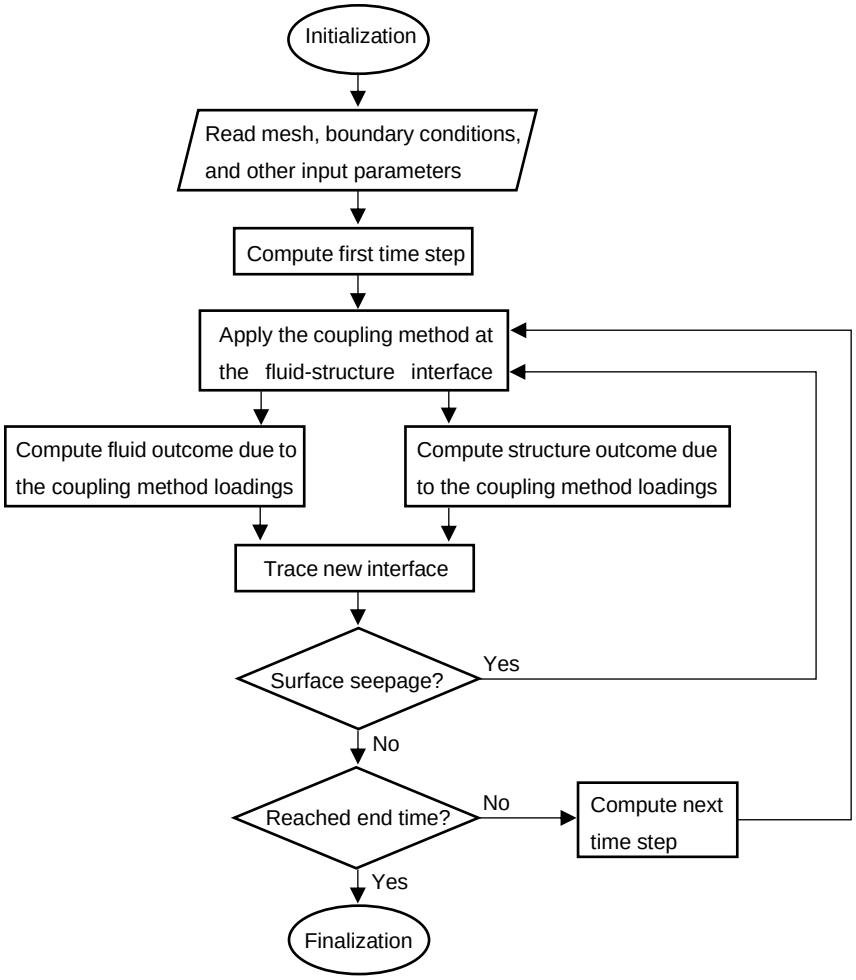

Figure 3.1: ALE algorithm flowchart.

The interaction between structure and fluid is performed using a coupling algorithm. In this case, the penalty method detailed by Aquelet et al. [3], was chosen as the coupling method. This method consists in using a spring system between the fluid nodes and the structure nodes at the fluid-structure interface. The penetration of the structural nodes through the fluid induce the so called “penalty forces” as there is a relative displacement on the spring of each connecting link. The penalty forces are then used to perform the calculations for the fluid and for the structure. These calculations are repeated until there is no penetration detected, only then the simulation will progress to the next time step.

3.2 Element type

For the ALE method in LS-Dyna, the fluid elements modeling the water and the air must be a specific element type, the ALE solid element, which is an eight-node brick element.

The structure mesh can be modeled either using only shell elements, only solid elements or a combination of both. Modeling the wedge mesh using only shell elements can result in a simpler model. Composite parts are often modeled using shell elements as they generally approximate well the “sheet” behavior (thickness much smaller than length and width).

As the object in study is composed by a composite sandwich structure, it could make sense to model at least the core material with solid elements, as the thickness can be high. Despite the added difficulty to get plausible values for the composite materials (especially in the out of plane direction) it was decided to model the whole wedge mesh in solid elements, also eight node structural bricks. This will enable to obtain structural results in the out of plane direction which is along the thickness of the structure, thus enabling to study the loadings along the thickness of the core. Modelling the structure in solid elements could also be useful in future work to address structural failure problems like delamination or core failure due to excessive compression stresses.

3.3 Materials

Unlike materials like steel, composites are known for having a lot of variation in terms of material properties. For this reason, it can be challenging to find plausible material properties without proper testing, especially in the out of plane direction.

The wedge modeled in this study is produced using composite materials and using the sandwich construction. The laminate schedule is presented in the next figure and it’s composed by three layers of 800 g/m^3 glass woven roving (0º/90º) at each skin being the layers oriented along and perpendicular to the wedge. The core material selected is a PVC foam with a density of 80 kg/m^3 with a thickness of 15 mm. The matrix for this laminate will be a vinylester resin.

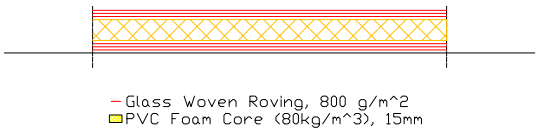

Figure 3.2: Composite laminate schedule.

Assuming that the composite was produced using the infusion technique, the Bureau Veritas rules [5] suggest that a mass fraction of 0.6 can be considered. With this assumption it's now possible to calculate several laminate properties.

All the material properties were obtained by a developed material calculator, with the results presented in Appendix A, which performs the calculations described in the previous chapter.

Materials must be defined in the computational model, in this case, the wedge is modeled with two materials, one for the core and the other for the skins. According to the rules [5], the core material can be approximated to an isotropic material with the following characteristics:

Table 3.1: Core material properties.

80 kg/m^3 PVC Foam Properties		
Density, ρ_c	80	kg/m^3
Elastic Modulus, E_c	67	MPa
Shear Modulus, G_c	31	MPa
Poisson Coefficient, υ_c	0.08	–

Regarding the material for the laminate skins, now being orthotropic, it can be approximated with the following properties:

Table 3.2: Skin material properties

Woven Roving Glass Vinylester Properties		
Density, ρ_{GRP}	1675	kg/m^3
Elastic Modulus (X direction), $E1_{GRP}$	18.31	GPa
Elastic Modulus (Y direction), $E2_{GRP}$	18.31	GPa
Elastic Modulus (Z direction), $E3_{GRP}$	5.83	GPa
Shear Modulus (X direction), $G1_{GRP}$	2.65	GPa
Shear Modulus (Y direction), $G2_{GRP}$	2.65	GPa
Shear Modulus (Z direction), $G3_{GRP}$	2.38	GPa
Poisson Coefficient (XY direction), $\upsilon 12_{GRP}$	0.072	–
Poisson Coefficient (XZ direction), $\upsilon 13_{GRP}$	0.226	–
Poisson Coefficient (YZ direction), $\upsilon 23_{GRP}$	0.226	–

As discussed previously, the wedge mesh will be composed of solid elements. Therefore, it's necessary to know the thickness of each skin.

The rules [5] present a table with information for each type of fiber and resins, suggesting that the density of E-glass type fibers can be approximated with 2.570 g/cm^3. The same goes for a vinylester resin, with a density of 1.100 g/cm^3. Considering three layers of a of 800 g/m^3 roving glass fibers, the total mass per square meters of dry reinforcements at each skin is 2400 g/m^3. Substituting all these parameters in equations (2.14) and (2.13) results a skin thickness of approximately 2.4 mm.

3.4 Model geometry

The two-dimension computational model has the geometry presented by figure 3.3, which also includes the global coordinate system. The geometry is composed by three body's, the air, the water and the wedge, whose geometry is presented in figure 3.4. Only half of the problem is modeled due to the symmetry by the wedge keel.

Regarding the domain, Luo et al. [13] suggests that the water domain dimensions should be at least five times the dimensions of the wedge, in both x and y directions. Has the wedge must be initially modeled above the air-water interface, the air domain height must be able to contain the wedge body with sufficient margin around the body. The air domain width should be equal to the water domain. The water and air sizes are fixed, being the water domain size 1250x700mm and the air domain size 1250x200mm.

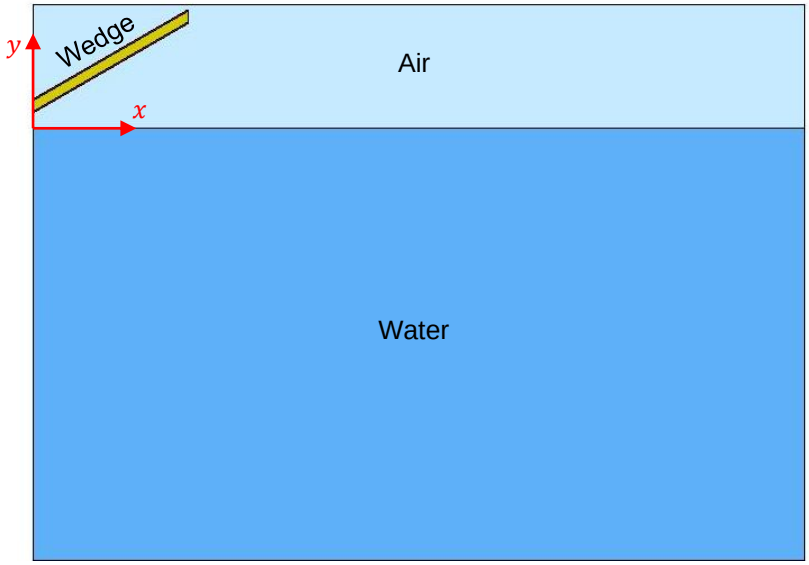

Figure 3.3: Model geometry.

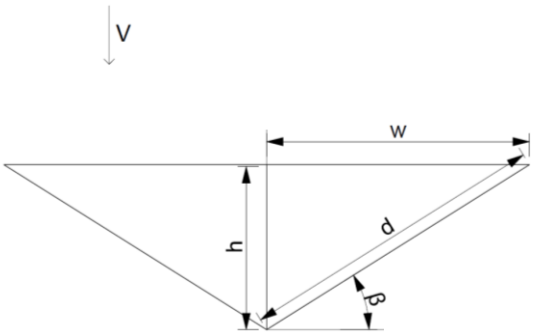

Figure 3.4: Wedge geometry

The wedge as a fixed length, d, of 300mm, being the deadrise angle, β, varied according to the simulation. The wedge's keel point is initially situated 25mm above water.

3.5 Mesh

The model mesh is very important in all the computational simulations as it is responsible for discretizing the problem governing equations into smaller cells/points. Authors with publications on this subject which are using computational approaches, for instance, Luo et al. [13], generally conclude that the mesh is one of the most important aspects of the computational methods. These previous researches show that the finer meshes will, generally, output results with increased precision. They also indicate that when the mesh is to coarse, the results may not be accurate enough, as the coarse mesh is not able to fully capture the finer physical effects occurring on the model. On the other hand, when the mesh is too small, the results accuracy can also be compromised due to the numerical round off errors occurring during the simulation.

To optimize the computing time, it's very important to use mesh refinements as can be seen in figure 3.5.

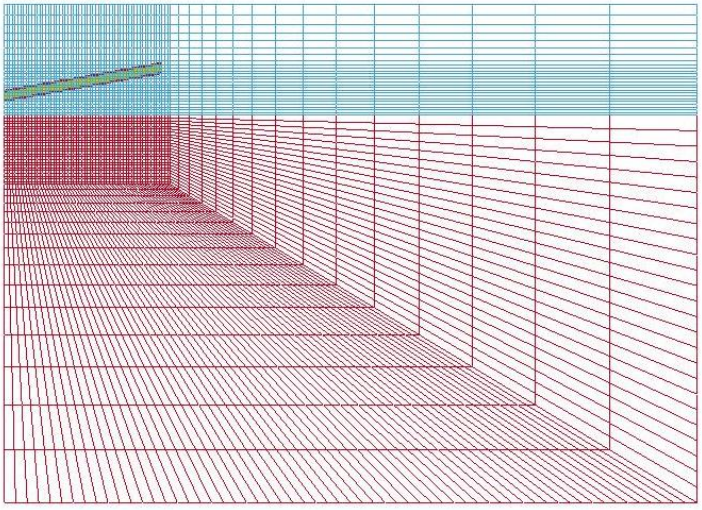

Figure 3.5: LS-Dyna computational mesh.

Once again it was used the same approach used by Luo et al. [13]. The water domain in which the wedge is expected to penetrate must be refined. This refinement should be done in both directions in a way that the elements contained by the refinement have the same length and width (square). The air domain must also contain a refinement, taking in account the effects of the jet flow and the surface elevation. The element size should then increase, progressively, between the mesh refinements regions and the outer boundaries of the model.

The influence of the element size is studied, hence, three meshes with different element sizes are produced. The fluid mesh (air and water) were set with elements having 5mm, 2.5mm and 1.25mm. Regarding the structure mesh, it's not possible to have square elements due to the constrains in thickness of the core and skin elements. However, it's important that the elements of the structure impacting the water have similar size to the fluid ones, to prevent leakage problems. The figure 3.6, presents as an example, the 5mm element size mesh used to model the wedge structure.

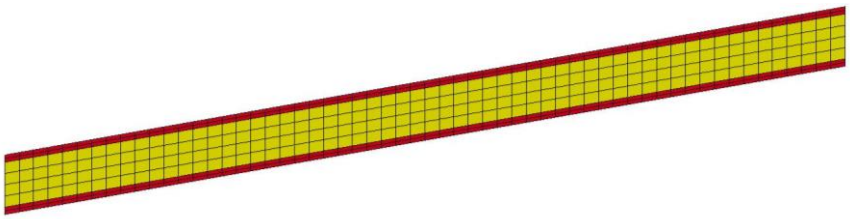

Figure 3.6: Wedge structure mesh.

3.6 Model loads and constrains

To achieve true two-dimensionality, all the body's in the model must only have one element in the Z directions. It's also necessary to constrain all the nodal displacement in the Z direction.

As explained before, only half of the wedge, air and water is modeled, due to the symmetry in the wedge geometry, which is useful to reduce computing time. However, it's necessary to impose the symmetric boundary condition on the symmetry plane wall of the model.

It's also necessary to add the non-reflecting boundary condition on the other outer walls of the model, to eliminate the effects of reflecting waves on these walls.

The loadings to the wedge are performed in the form of velocity. Velocity inputs are added to the keel point and to the other end of the wedge, these can be constant, free drop or with a velocity curve, depending on the simulation case in study. Additionally, in the first time-step, initial velocity is added to all nodes of the wedge. Running the simulation without this initial condition resulted in vibrations across the wedge in the first few moments, therefore it's important to impose this condition in order to reduce the difference in velocities along the wedge prior to the impact.

The study presented by Luo et al. [13] indicate that the acceleration of gravity can be neglected when considering the drop tests. It was also concluded that this assumption was only valid for wedge type geometries. For this reason, the influence of the acceleration of gravity to the drop velocity was neglected in the free drop simulations.

3.7 Equation of state

As the Eulerian fluid materials are defined as null, it´s necessary to establish an equation of state for each of them.

3.7.1 Gruneisen EOS

For the water, the Gruneisen equation of state is chosen. The Gruneisen equation of state with cubic shock velocity as function of particle velocity defines pressure as:

$$p = \frac{\rho_0 C^2 \mu \left[1 + \left(1 - \frac{\gamma_0}{2}\right)\mu - \frac{a}{2}\mu^2\right]}{\left[1 - (S_1 - 1)\mu - S_2 \frac{\mu^2}{\mu + 1} - S_3 \frac{\mu^3}{(\mu + 1)^2}\right]^2} + (\gamma_0 + a\mu)E \tag{3.1}$$

where *C* is the curve intercept; S_1, S_2 and S_3 are the slope coefficients and γ_0 is the Gruneisen gamma coefficients.

Wang and Guedes Soares [23] suggest that, for water, the following coefficients can be used for the Gruneisen equation of state:

Table 3.3: Gruneisen EOS parameters.

Item	*ρ (kg/m³)*	*C (m/s)*	S_1	S_2	S_3	γ_0
Water	1000	1480	1.92	−0.096	0	0.1

3.7.2 Linear Polynomial EOS

For the air, the linear polynomial equation of state, was adopted. The pressure is defined by the following polynomial:

$$p = C_0 + C_1\mu + C_2\mu^2 + C_3\mu^3 + (C_4 + C_5\mu + C_6\mu^2)E \tag{3.2}$$

where *E* is the internal energy, μ is the ratio of the current density to the reference density and C_1 to C_6 are constants.

It has been shown that the linear polynomial equation of state can be used to model a gas by imposing the following:

$$C_0 = C_1 = C_2 = C_3 = C_6 = 0 \tag{3.3}$$

and,

$$C_4 = C_5 = \gamma - 1 \tag{3.4}$$

where γ is the ratio of specific heat, which, for the air at ambient temperature can be taken as 1.4.

The following table resumes the coefficients to be used with the linear polynomial equation of state:

Table 3.4: Linear polynomial EOS parameters.

Item	C_0	C_1	C_2	C_3	C_4	C_5	C_6
Air	0	0	0	0	0.4	0.4	0

3.8 Local coordinate system

In order to obtain the stress and displacement results of the structure in relation to the right coordinate system, its necessary to present an additional local coordinate system at the structure.

As can be seen in figure 3.7, the global coordinate system is established at the symmetry line in the interface between air and water. Since the results for the structure should be presented in relation to the wedge impact surface, it´s necessary to define in LS-Dyna a coordinate system at the keel of the wedge and with an inclination in relation to the global coordinate system that is equal to the wedge deadrise. Another important aspect of this local coordinate system is that it should move with the wedge along the simulation.

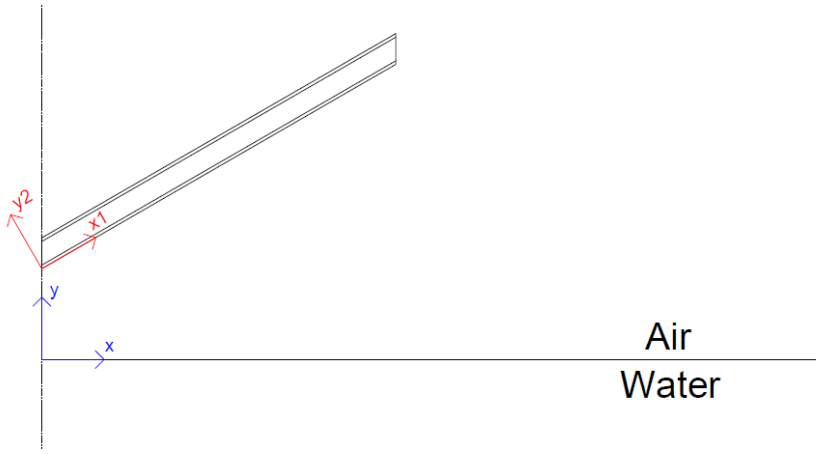

Figure 3.7: Local coordinate system.

3.9 Model setup

In order to obtain good results without excessive computational time it's necessary to tune the parameters described next.

3.9.1 Simulation time

The simulation time should be one that, not only, allows for the whole problem to be simulated but also not to run the simulation in excess has this will result in unnecessary computing time.

In this problem, it´s considered the body will impact the water with constant velocity, therefore the simulation time can be calculated based on the velocity and on the geometry of the wedge, which was presented in Figure 3.4. The simulation time is such that the wedge must be fully immersed, thus the distance to be travelled, *hw*, is equal to the height, *h,* presented in the previous figure 3.4 plus the 25mm margin to the keel:

$$hw = h + 0.025 \tag{3.5}$$

The wedge height, *h,* is obtained by trigonometry in relation to the wedge length and the deadrise:

$$h = d * \sin\beta \tag{3.6}$$

It's convenient to add a 10% margin to the simulation time, to ensure that the problem is fully captured. With the velocity relation and substituting equations (3.5) and (3.6), the simulation time can be obtained by:

$$t = 1.1 * \left(\frac{d * \cos\beta + 0.025}{V}\right) \tag{3.7}$$

3.9.2 Solver

Using the double-precision solver instead of the single precision one, the simulation time will increase significantly, however it's important to run the simulations with the double-precision solver, as the results produced by this solver are smoother and more consistent. This may not be noticeable with big mesh sizes, but with smaller meshes the difference starts to be relevant. The difference between each solver will be demonstrated later.

3.9.3 Time step

At each time step, calculations must be performed to all the nodes. Since the calculations at each node are dependent on each other, the solver starts the calculation at a certain node and then propagates the calculations to rest of the mesh, creating a wave-like effect.

The critical time step is the time increment in the solution that enables the calculations to be performed to all nodes without being affected by the calculations from the next time step. This time increment is automatically calculated by LS-Dyna, but it´s possible to setup a scale factor based on the critical time step. The default value for the time step scale factor is 0.9. Reducing this factor can solve instability issues caused by the fast-evolving nature of the simulation but will result in a longer computational time.

Later, a parametric study is performed to the time step scale factor, demonstrating the impact of different values on the simulation results.

3.9.4 Penalty factor

As explained earlier, the software deals with the fluid-structure interface using a coupling method that can be approximated to a spring system. In order to calculate these coupling forces, LS-Dyna automatically estimates the stiffness in the spring-like system.

In similarity to the time step, it is possible to setup a scale factor to the estimated stiffness. With this feature it's possible to control how strong is the connection between the fluid and structure nodes which can result in big changes to the final results. LS-Dyna provides a specific output to quantify the energy absorbed by the coupling mechanism which is the contact energy output. The penalty factor (PFAC) should be tuned in a way that the contact energy absorbed at the coupling interface is small when compared to the internal energy, which is the energy contained in the system. It's possible for LS-Dyna to output a result with negative contact energy. This indicates that the model needs better parameter tuning and can also indicate other problems like leakage. Adopting a low value for the penalty factor results in a very stiff structure which induces forces on the structure that are not real. These can be easily noticed with the increase of the contact energy. On the other hand, an higher penalty factor results

in undesired oscillations in the fluid structure interface and can result in leakage. A good compromise for moderate deadrise and impact velocities is generally obtained by using 0.01 as the standard value for the penalty factor.

3.9.5 Coupling points

The number of coupling points (NQUAD) determines how many points, equally divided, in each Lagrangian segment that are dedicated to the coupling algorithm. During the simulation, the algorithm searches for any ALE elements crossing the coupling points interface, applying the coupling forces to these elements.

When the number of coupling points is small to the given problem, leakage may occur at the fluid structure interface. This can happen for instant, when the Lagrangian elements are larger than the ALE ones. It can also occur when the structure deformation is larger.

Similar to the PFAC, a higher number of coupling points increases simulation time but reduces leakage at the fluid structure interface. Three coupling points are generally sufficient to model the fluid structure interface.

3.9.6 General Remarks

As explained earlier, the setup parameters presented above are generally adequate for moderate velocities and deadrises, but each simulation must be checked in terms of stability and validity, as the lower deadrises and higher impact velocities will often present problems like leakage, which should be solved by increasing the number of coupling points value or by lowering the penalty factor.

4. Rigid body model validation

Just like any other computational, analytical or experimental model, one of the first and most important aspects of the whole model is its own validation. All the results obtained when using a new model, should not be taken as plausible results if the model was not subjected through an extensive validation study.

This chapter addresses the validation of the model, focusing in the fluid component of the model, hence, the influence of the structure and the hydroelasticity is not considered by using a rigid body model. The validation is performed by comparison of the results with other know experimental and numerical results from authors like Zhao et al. [27] or Mei et al. [14]. Comparisons are also made in relation to the Luo et al. [13] research, on which this rigid body model is based, being the major difference, the element type adopted in each model.

4.1 Validation model

The validation of the model is performed by simulating the model with given input parameters, which are the ones which approximate the most the simulations and experiments that will be used as comparison. This first part of the validation is focused on the fluid part of the model, for this reason, the results used for the model validation are the ones related with the fluid component of the simulation, like the pressure and slamming forces acting on the body. The results obtained from the simulation include the pressure distribution along the wedge at different time instants and the time histories of the pressure and the slamming force.

The body used for the validation is similar, in geometry, to the ones used for comparing the results, as can be seen in Figure 4.1, which corresponds to the model used by Zhao et al. [27] when conducting their experiments.

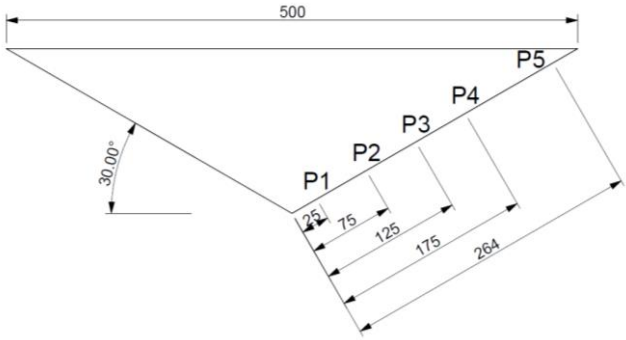

Figure 4.1: Geometry of the experimental model and gauge location used in Zhao´s experiments.

Another important aspect to isolate the fluid component of the simulation is to eliminate the effects of hydroelasticity. For this reason, the wedge is modeled with the composite materials, but the structural displacement is locked, turning the wedge into a rigid body.

Table 4.1 describes the input parameters used in the simulation. Some of these parameters, like the mesh size, the penalty factor and the time step factor were chosen based in a parametric study which is presented later.

Table 4.1: Input parameters used in the rigid model validation

Rigid body validation model parameters		
Body model	Rigid	
Velocity model	Free-falling	
Initial velocity	6.15	m/s
Deadrise	30	degrees
Mesh size	1.25	mm
Penalty factor, PFAC	0.01	–
Time step factor	0.9	–
Nº of coupling points	3	–
Simulation time	0.03	s

The materials adopted for the wedge´s structure are the ones presented in the previous chapter, although, since the wedge body is modeled as being rigid, the material properties do not influence the simulation results.

4.2 Simulation results overview

Before starting to compare the results obtained with other experiments, simulations or analytical approaches, it's important to analyze the simulation and identify the most important physical effects occurring during the simulation.

Figure 4.2 illustrates the variation of the average pressure acting on the wedge along the simulation time. The keel point only touches the surface of the water in time instant of 0.0039s but, for the sake of simplicity, all the results presented next set this time instant to zero.

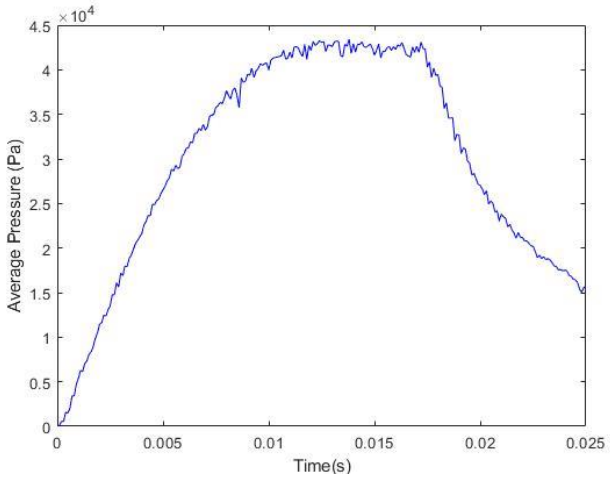

Figure 4.2: Average pressure time history.

Looking to the past figure, one can easily notice the pressure increase during the water entry, which then stabilizes and then abruptly drops. This dropping phenomenon is the flow separation which occurs when the water up-rise reaches the end of the wedge as can be seen in the next set of figures:

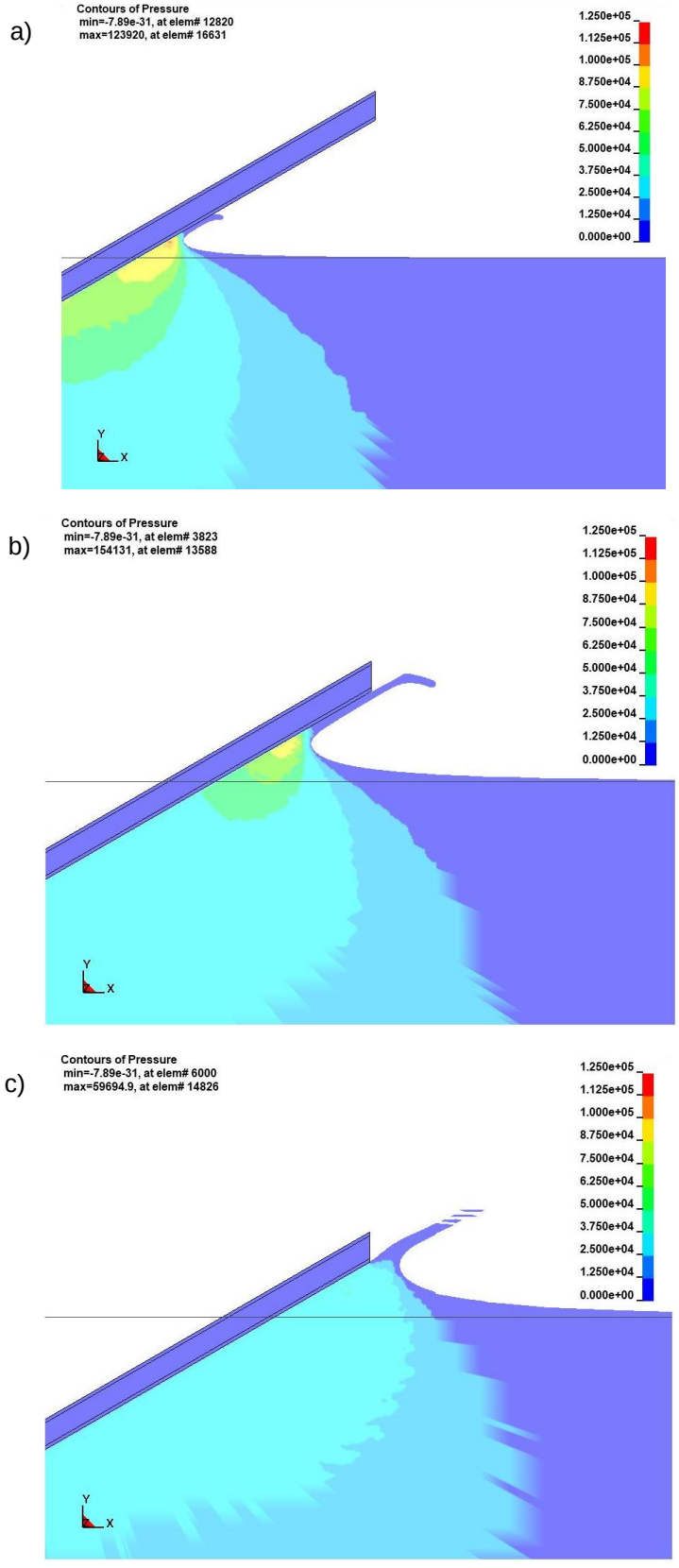

Figure 4.3: Water entry and pressure contour. a) t1 = 0.0063s; b) t2 = 0.0135s; c) t3 = 0.0189s

The previous figures illustrate the surface elevation with the pressure contours at different time instant. The first time instant, t1 = 0.0063s, is taken during the pressure build-up process and the other time instants, t2 = 0.0135s and t3 = 0.0189s, are taken before and after flow separation, respectively.

Comparing the time instants before and after flow separation, one can easily notice the pressure drop and also the pressure equalization along the wedge, after the flow separation. Also, the pressure at the flow jet created by the water up-rise is negligible which confirms some of the theory's proposed in this subject.

From the figures, one can also conclude that there is no visible leakage in the wedge surface. This can also be checked by observing the sliding energy data, which is explained in the parametric study chapter.

After presenting the average pressuring acting on the wedge it´s also important to present the pressure variation along the wedge at fixed time instants. This time, the pressure is presented in the form of the non-dimensional pressure coefficient which can be obtained using the formula (2.7) given earlier. This coefficient takes in account the dropping velocity, which in this case, it´s not constant. Figure 4.4 presents the velocity variation that can be used to calculate the pressure coefficient.

In the Figure 4.5, the position along the wedge is also presented in the non-dimensional form, being zero the keel point and one the end of the wedge.

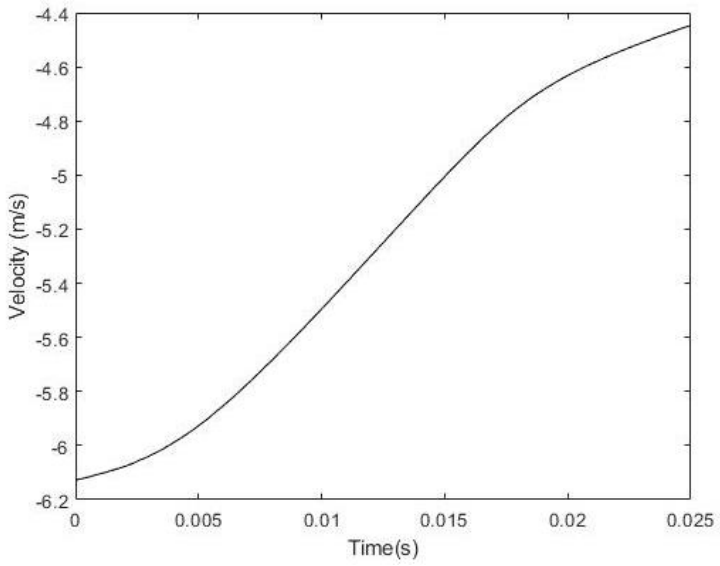

Figure 4.4: Drop velocity variation during the simulation.

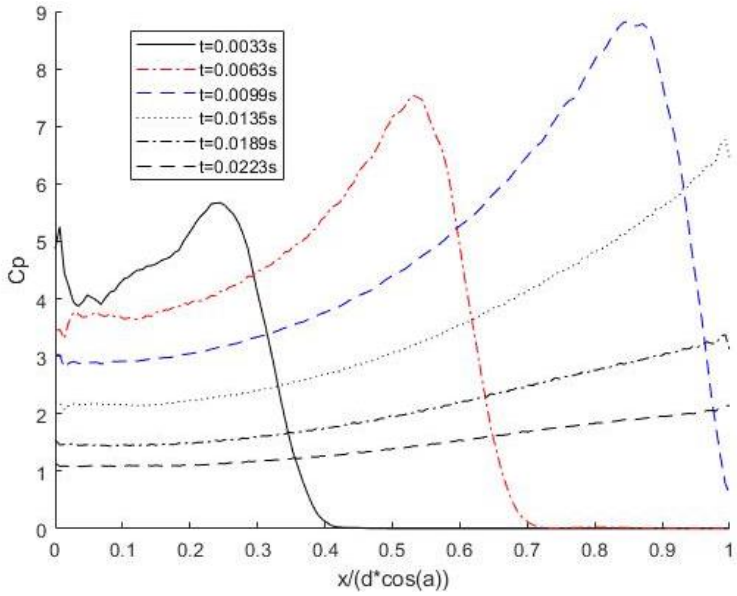

Figure 4.5: Pressure distribution along the wedge at different time instants.

The pressure distribution demonstrated in the previous figure includes the time instants presented earlier. Additionally, three more instants are presented. The first four occur before flow separation and the remaining two after flow separation.

One can notice that the pressure keeps rising during the water entry until the flow separation. It´s also possible to observe that, before the flow separation, the maximum pressure is always situated near the end of the water up-rise (or where the water jet forms) and that its value increases as the wedge sinks.

After the flow separation, the pressure acting on the wedge not only starts to decrease but also tends to equalize along the wedge as can be observed in the latter time instants of Figure 4.5.

4.3 Results comparison

After the brief discussion of the results, it´s comparison with other theories and methods is followed.

The most relevant theories which can be applied to this study is the one from Wagner [22] and Mei et al. [14]. On the experimental side, this validation model simulates the water entry of the wedge in the same conditions from Zhao et al. [27] experiments. Being this study based on Luo et al. [13] research, their results are also included.

4.3.1 Velocity profile

As referred previously the velocity case in this validation model is free dropping, therefore the velocity is not constant during the simulation. Instead of adapting the wedge mass and inertia to correctly model the drop velocity behavior, it was decided to use the same velocity profile occurring in Luo et al. [13] simulations.

Figure 4.6 presents the comparison of the velocity profiles observed in the numerical and experimental simulations. The velocity profile observed in the LS-Dyna results is coincident with the one presented

by Luo et al. [13], however they are both slower than the one observed in Zhao et al. [27] experiments. This difference can induce some differences in the pressure results that will be presented next.

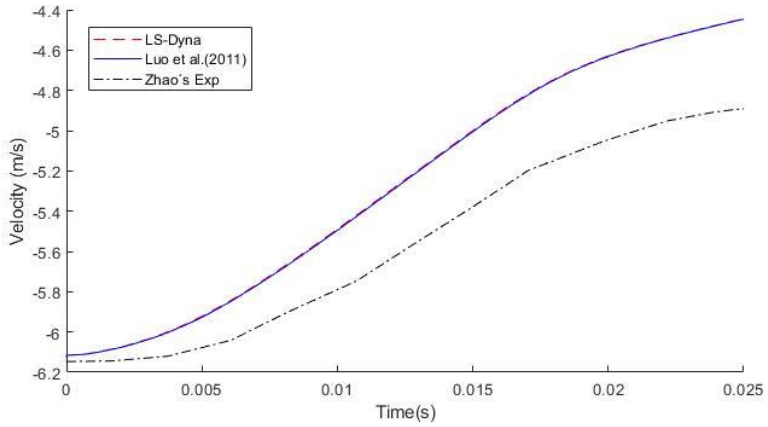

Figure 4.6: Velocity profile comparison.

4.3.2 Total slamming forces

Figure 4.7 presents the comparison of the total slamming forces results. The comparison includes all the analytical, experimental and numerical results taken from the research of the authors listed above.

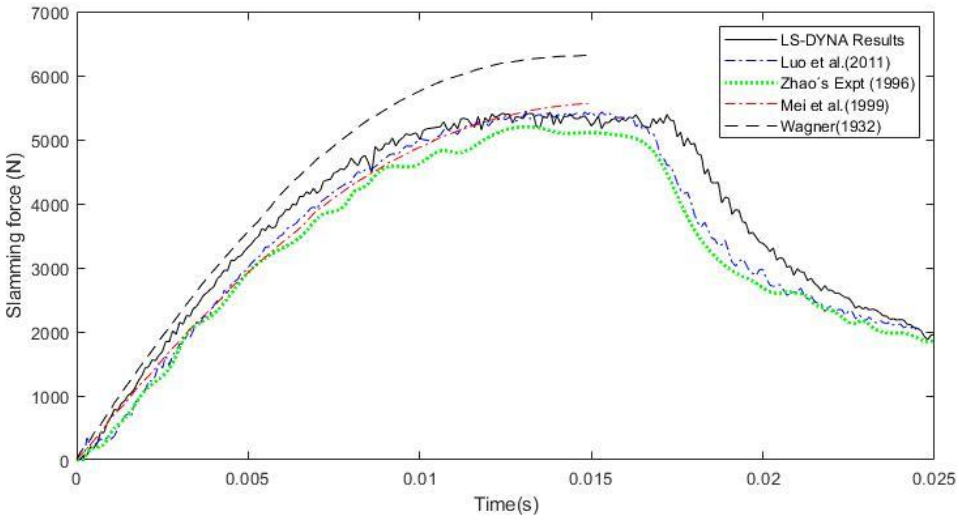

Figure 4.7: Total slamming forces comparison.

As can be seen in the previous figure, the results agree very well with each other, with only the Wagner´s results overestimating the force results. This is a good indication regarding the validation of the model. Wagner [22] and Mei et al. [14] results end earlier, since they do not include the flow separation effect.

One can notice a small difference between the results obtained in LS-Dyna to the ones from Luo et al. [13], as the forces on this model hold their maximum value longer before starting to decrease due to the flow separation. This can be explained due to the small difference in the wedge length.

Additionally, it was decided to run an additional simulation considering the velocity curve observed in Zhao et al. [27] experiments, which was presented in Figure 4.6. The results for the slamming force time history are presented in Figure 4.8, along with the LS-Dyna computational results and Zhao et al. [27] experimental results:

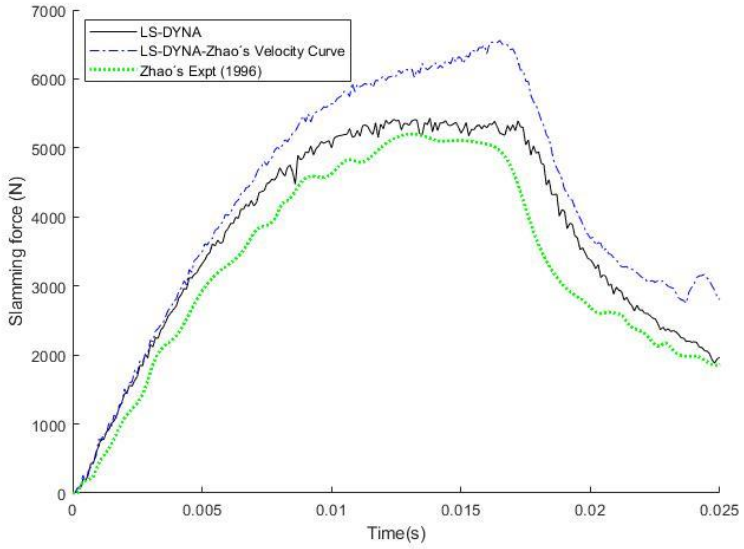

Figure 4.8: Slamming forces comparison adopting Zhao´s velocity curve.

The results indicate an increase in the slamming forces when considering Zhao´s experimental entry velocity curve in relation to the previous LS-Dyna results. This was expected since the entry velocity curve observed in Zhao et al. [27] experiments is larger than the first one adopted in this model, hence the increase in the slamming forces.

Despite this behavior being expected due to the previous results, the physical explanation for this increase is due to the differences in the model, that in the case of the LS-Dyna simulations, being a two dimensional model, do not take in account the pressures losses in the third dimension that are present on the physical experiments. Zhao et al. [27] research also appointed to these differences by comparing the experimental results to other numerical approaches available at that time, having concluded that the differences in the slamming forces can go up to 20%.

4.3.3 Pressure distribution at given time instants

Zhao´s research also included results for the pressure distribution along the wedge at different time instants. Figure 4.8 presents the comparison of results in the pressure distribution. The time at which the results are taken refers to an instant before the flow separation, which in this case is the same presented in the earlier figures, t2 = 0.0135s.

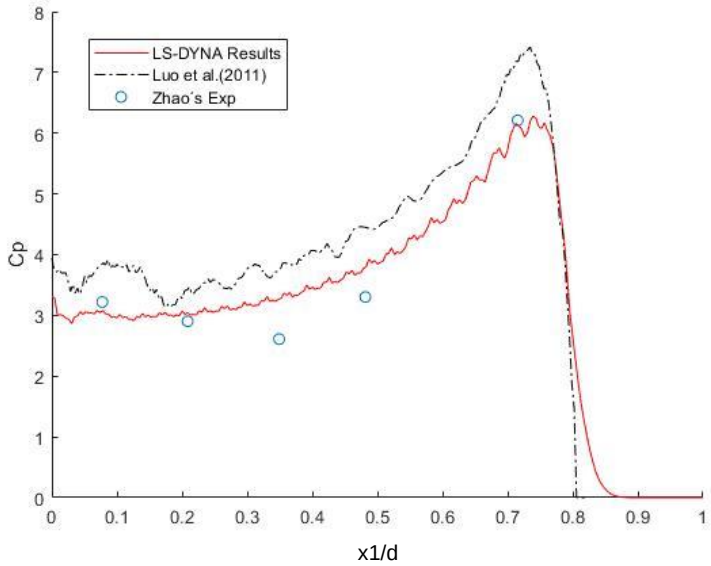

Figure 4.9: Pressure distribution along the wedge before slow separation.

The figure illustrates the differences in the pressure coefficient between the simulation and Zhao´s experiments. The results from LS-Dyna agree very well with the other results, with the peak value being similar to the one observed in Zhao´s experiments. Overall the results obtained by Luo et al. [13] are slightly larger.

In general, one can conclude that the pressure variation is similar among the different results, having the numerical method presented by Luo et al. [13] higher values. Better tuning of the model parameters could, probably, approximate more the two numerical results.

4.3.4 Pressure time history at given locations

Zhao et al. [27] included in their experimental model five pressure sensors installed at the locations presented earlier in the Figure 4.1. In this case, it was implemented in the LS-Dyna model one pressure sensor for each element of the wedge impacting surface.

After selecting the elements in the model and the respective pressure sensors corresponding to the locations proposed by Zhao et al. [27], it's possible to obtain the time histories presented in the next set of figures:

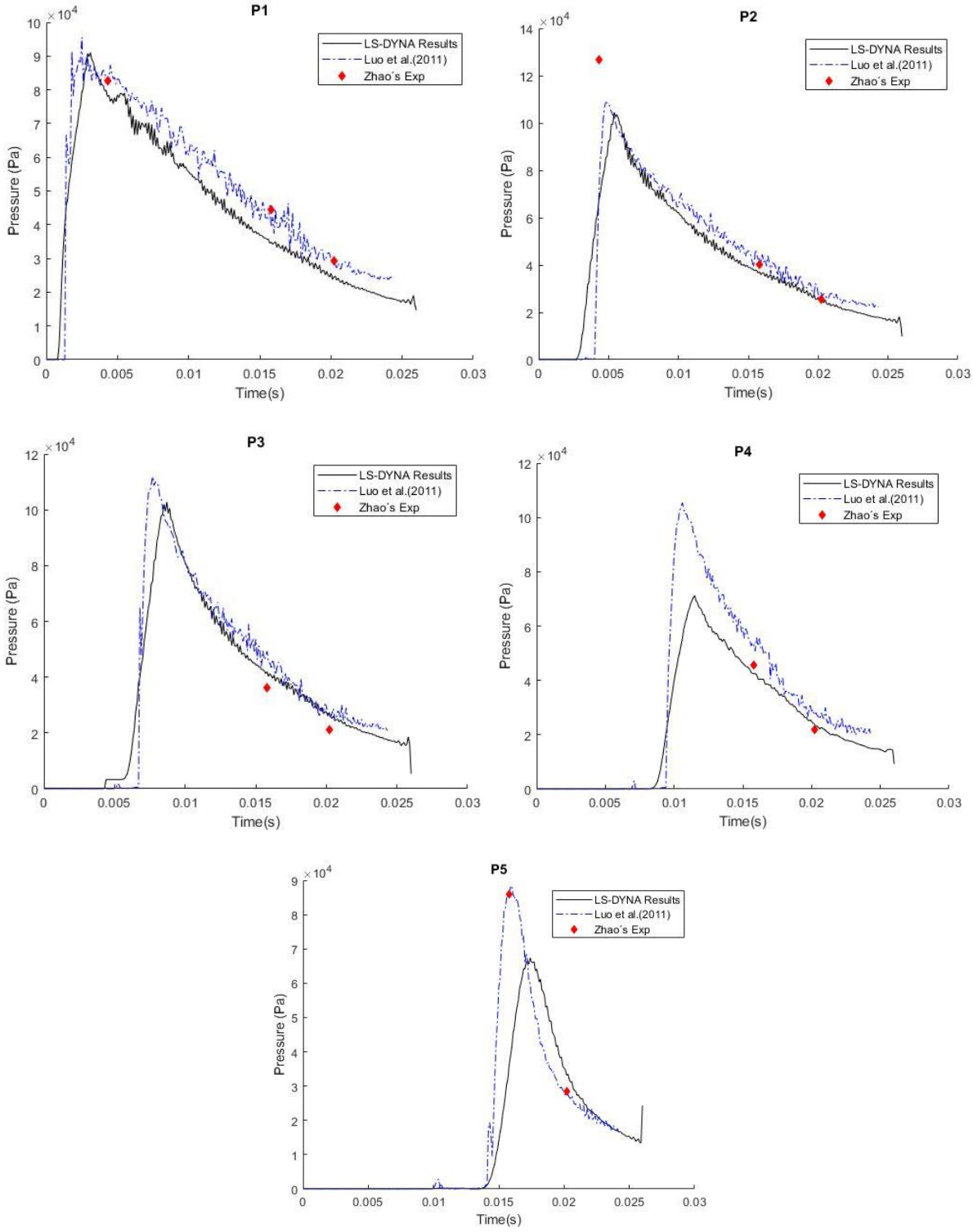

Figure 4.10: Pressure time histories at different locations.

Once again, looking to the time histories presented in Figure 4.9, the results show that there is good similarity between the experimental and numerical results, even some of the experimental results are coincident with the ones obtained in LS-Dyna.

In the pressure points P3 and P4 both numerical methods obtained in LS-Dyna show a slightly variation from Zhao´s experimental results, although the patterns developed by the results are the same. In the

case of the pressure points P1 and P5 the results obtained in LS-Dyna are coincident with the experimental results obtained by Zhao et al. [27]. In the pressure point P2, the results also show good agreement, having only revealed that the predicted peak pressure by the numerical methods is lower than the one obtained experimental. This can be caused if the mesh is note fine enough to capture the peak value or if the capturing frequency is not high enough.

4.3.5 Maximum pressure coefficient and deadrise angle

The last comparison in this model validation is the one which relates the different results obtained for the variation the maximum value of the non-dimensional pressure coefficient with the change of the deadrise angle.

In this simulation, the input velocity is not free dropping but is fixed to 6.15 m/s. Additionally, the simulation was performed using two new bodies with different deadrises angles, 10º and 20º. The other input parameters remained the same.

This comparison, which is presented in the Figure 4.70, includes the numerical results obtained by Luo et al. [13], the analytical results which can be obtained by the Wagner [22] formulation and both results obtained from the empirical formulations, explained earlier, which are proposed by Stavovy and Chuang [18], and Ochi and Motter [15].

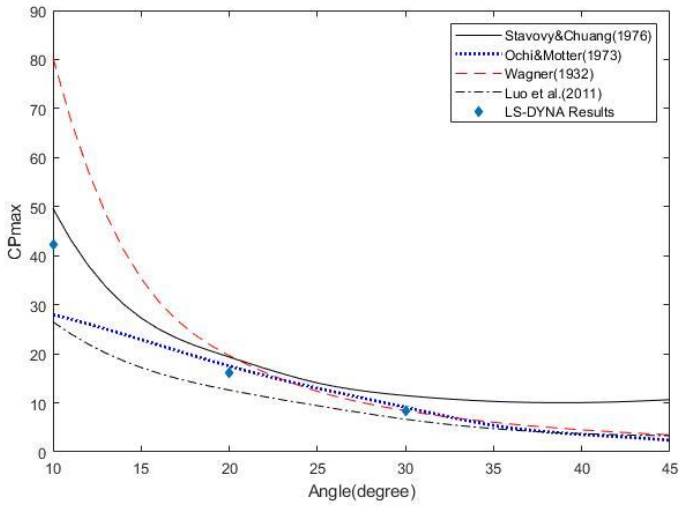

Figure 4.11: Variation of the maximum pressure coefficient with the deadrise angle.

The previous figure illustrates the differences between the results. One can rapidly conclude that all the methods show good agreement with each other when the deadrise angle is large. However, the small deadrise angles leads to big differences in the results. This is somehow expected, since the small deadrises are often harder to numerically simulate due to the fast-evolving nature of the problem. The results obtained in LS-Dyna for 20º and 30º deadrise angles is very similar to the other results. Despite the 10º case result is fitting between the other results, it's difficult to conclude its validity since all the results are very different between each other.

4.4 Rigid body validation final discussion

The comparison of the results obtained by LS-Dyna for the 30º deadrise angle wedge, free drop case with the other available numerical, experimental and analytical results show that this numerical formulation can successfully model the slamming problem when applied to a wedge.

Overall, the simulations show that the pressures results are similar when compared to the research proposed by Luo et al. [13]. The small differences can be, as explained earlier, due to a small difference in the wedge geometry, other simulation parameters or even by the differences in the element type. Another plausible reason is related to the fact that it was not possible to capture the complete values at the fluid structure interface, since the results presented are obtained from the averages resulting in each element.

When compared to the experimental results proposed by Zhao et al. [27], the results with the corrected velocity curve are slightly larger. In this case, the difference can be explained by the three-dimensional effects that can influence the experimental results since the numerical results proposed by this study apply to the two-dimension wedge, which can be approximated to an infinite length three-dimensional wedge.

This page was intentionally left blank

5. Flexible composite body model validation

The previous chapter addressed the rigid body model validation, in which the results were compared with other analytical and numerical approaches. Essentially, only the fluid part of the model was validated, since it was adopted the rigid body structure which eliminates any effects cause by hydroelasticity.

In this chapter, another model validation is performed based on the experiments proposed by Hassoon et al. [10]. The objective of this chapter is to validate the finite element part of the model as well as the model behavior when dealing with hydroelasticity.

5.1 Validation model

To proceed with the validation, the numerical model is built using the same geometry, materials and loadings as the ones presented on Hassoon et al. [10] experimental research. The results obtained from this simulation are then compared with the ones obtained on the experiments.

The wedge geometry adopted on the experiments was composed by two sandwich plates fixed at both ends and at the keel. The length of each plate was 500mm and the deadrise is fixed for all the experiences at 10º. The two sandwich plates were composed by two FRP skins with a thickness of 7mm each and a 20mm PVC foam core. Additionally, each plate had a depth of 250mm. This third dimension is not considered in the model geometry since it is modeled in two dimensions, but the depth must be taken in account when comparing results that are dependent of the impact area, which is the case of the slamming forces.

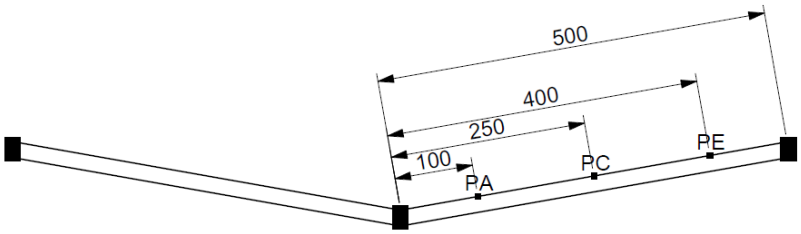

Figure 5.1: Experimental model adopted by Hassoon et al. [10].

Figure 5.1 presents the wedge adopted by Hassoon et al. [10], including its fixation scheme and the locations of the strain gauges in which the experimental results are based.

The plates subjected to the experiments, also made from the sandwich construction, had the following skin and core mechanical properties, which will be adapted in the numerical model:

Table 5.1: Core foam properties used by Hassoon et al. [10].

80 kg/m³ PVC Foam Properties		
Density, $\rho_{c_{ver}}$	80	kg/m³
Elastic Modulus, $E_{c_{ver}}$	77	MPa
Shear Modulus, $G_{c_{ver}}$	29	MPa
Poisson Coefficient, $\upsilon_{c_{ver}}$	0.3	–

Table 5.2: GRP skin properties used by Hassoon et al. [10].

Glass Vinylester Properties		
Density, $\rho_{GRP_{ver}}$	1960	kg/m³
Elastic Modulus (X direction), $E1_{GRP_{ver}}$	48.16	GPa
Elastic Modulus (Y direction), $E2_{GRP_{ver}}$	11.21	GPa
Elastic Modulus (Z direction), $E3_{GRP_{ver}}$	11.21	GPa
Shear Modulus (X direction), $G1_{GRP_{ver}}$	4.42	GPa
Shear Modulus (Y direction), $G2_{GRP_{ver}}$	4.42	GPa
Shear Modulus (Z direction), $G3_{GRP_{ver}}$	9	GPa
Poisson Coefficient (XY direction), $\upsilon 12_{GRP_{ver}}$	0.274	–
Poisson Coefficient (XZ direction), $\upsilon 13_{GRP_{ver}}$	0.274	–
Poisson Coefficient (YZ direction), $\upsilon 23_{GRP_{ver}}$	0.096	–

Due to the physical restrains in the experimental model setup, it was not possible for Hasson et al. [10] experiments to be run at constant velocity. For this reason, one should guarantee that this validation simulation is performed with the same velocity as the experimental tests.

Figure 5.2 presents the velocity curve observed during Hassoon et al. [10] experiments. This velocity profile should be adopted in the validation model.

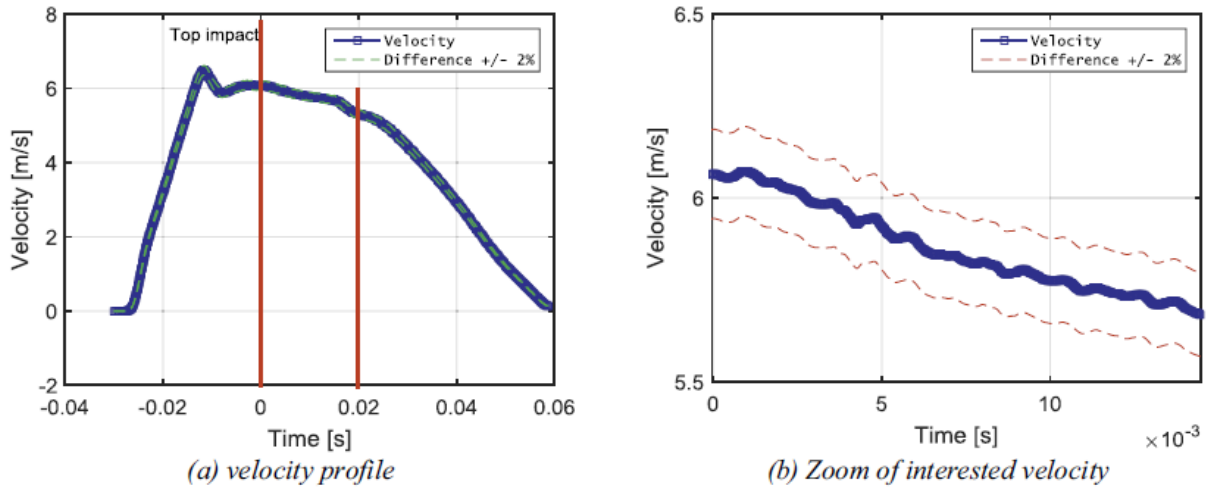

(a) velocity profile *(b) Zoom of interested velocity*

Figure 5.2: Velocity curve observed during Hassoon et al. [10] experiments.

Due to the nature of the problem, it was not possible to get good results in the first simulations, as they presented leakage through the fluid-structure interface, as can be observed in Figure 5.3. In the same figure one can observe that the leakage does not seem to be of great importance as the pressure contour on the leaked fluid is negligible, however, the contact energy on this simulation is negative. To solve this problem, the number of coupling points was increased, as well as the time step factor decreased and the penalty factor also had to be adjusted.

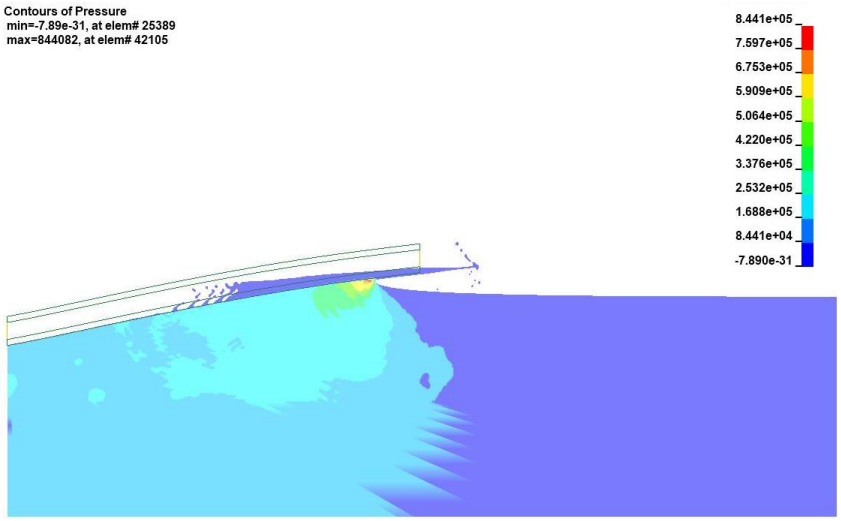

Figure 5.3: Leakage occurring during the water entry.

As presented on Table 5.3, which is the resume of the input parameters. The simulations were performed using a model with 1.25mm mesh. Since the model is bigger than the other computational models presented in this thesis and the time step factor was decreased, the computational time increased, substantially, to ten hours.

Table 5.3: Input parameters used in the flexible composite body validation model.

Flexible composite body validation model parameters		
Body model	Flexible	
Velocity model	Variable	
Initial velocity	6.4	m/s
Deadrise	10	degrees
Mesh size	1.25	mm
Penalty factor, PFAC	0.005	–
Time step factor	0.4	–
Nº of coupling points	5	–
Simulation time	0.022	s

5.2 Results comparison

The main results presented by Hassoon et al. [10] research is the vertical slamming force acting on the wedge and the strain measured in the sandwich plate via the different strain gauges. Hasson et al. [10] research not only includes the experimental tests but also presents a comparison with a computational model implemented in Abaqus.

5.2.1 Vertical slamming force

The next figure presents the results for the vertical slamming force acting on the sandwich plate:

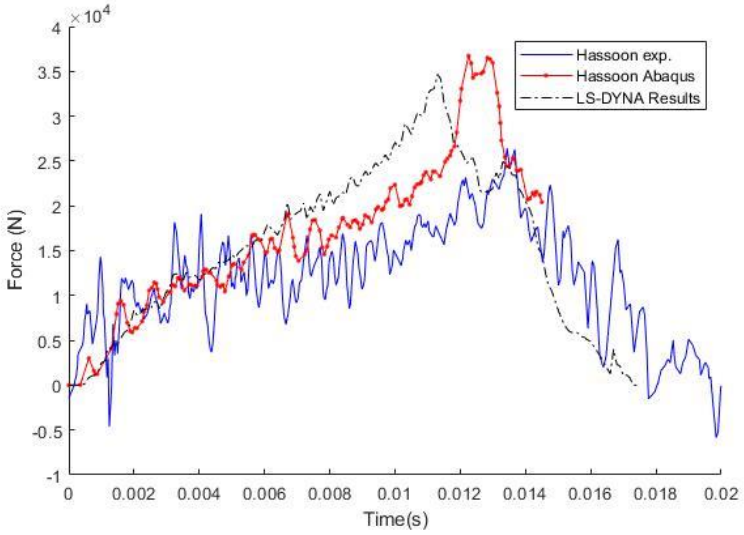

Figure 5.4: Vertical slamming force comparison.

Despite some difference in the middle part of the water entry, the results show good agreement. Both computational models show higher peak force when compared with the experimental result. There are a number of factors that can induce this difference, for instance, the effect of the third dimension presented in the experiments, which generally results in a loss of pressure when compared to the infinite length two-dimensional problem.

5.2.2 Strain comparison

Since the computational model presented in this chapter uses the same material and geometry as the experiments, the structural behavior should be similar in both cases.

As explained earlier, the experiments included three strain gauges installed at the locations demonstrated by Figure 5.1. In the case of the computational model, the strain can be taken from the elements output results.

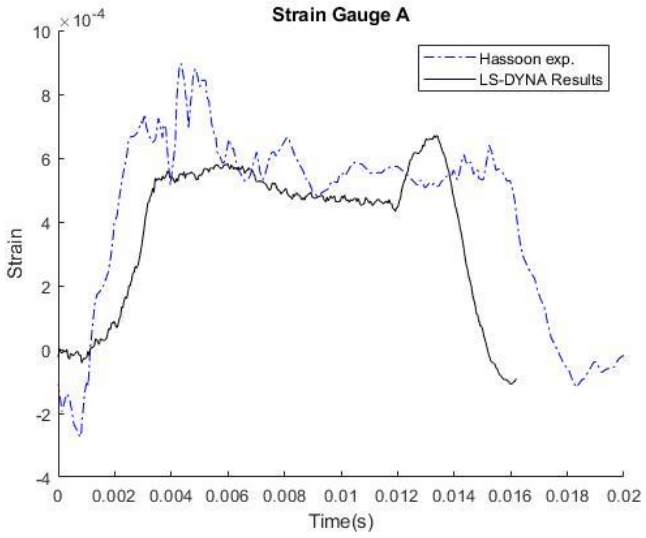

Figure 5.5: Strain comparison at position PA.

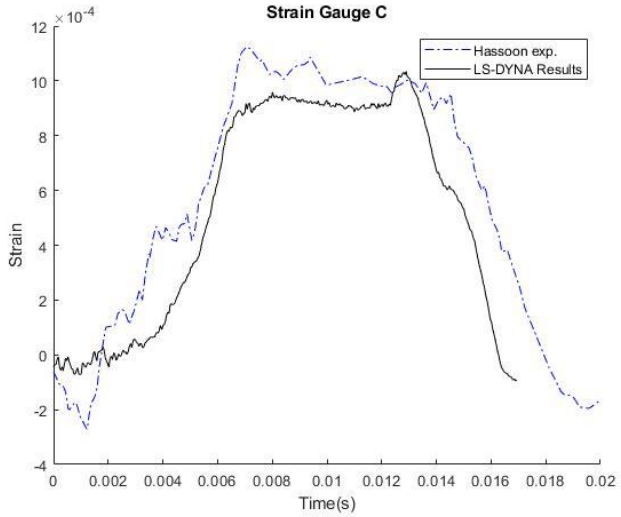

Figure 5.6: Strain comparison at position PC.

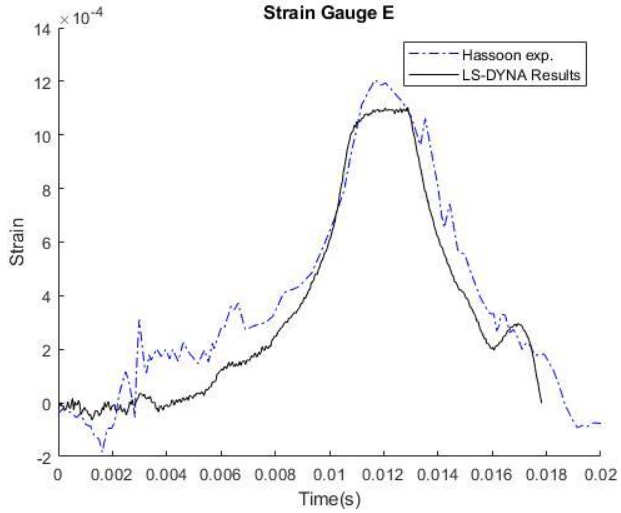

Figure 5.7: Strain comparison at position PE.

The figures presented above demonstrate the strain comparison between the experiments and the LS-Dyna results.

In general, the results show very good correlation, especially when comparing the strain gauges C and E. Overall, the strain results obtained in the experiments tend to present themselves earlier during the time history and hold their value longer. This effect can be explained by factors like the strain gauges positioning or other experimental effects, has these are devices which are very sensitive and that can, sometimes, induce errors when not properly aligned or calibrated.

5.3 Flexible composite body validation final discussion

The comparison of the results obtained by LS-Dyna, for the 10º deadrise angle flexible composite wedge using the geometry and materials proposed by Hassoon et al. [10] research with the numerical and experimental results presented on the same research, show that this formulation can successfully model the slamming problem applied to a composite made wedge.

Overall the results show good agreement between themselves, with some small differences in the peak forces and strain results. This can be explained by the differences in the models presented in this chapter. The LS-Dyna model is a numerical approach that differs to the experimental model proposed Hassoon et al. [10] due to the third dimension associated effects. The same research also presents a comparison with another numerical approach in which the third dimension is considered, however the velocity profile was not modeled, hence the differences in the results.

6. Parametric study

As with any other numerical simulation, there are important input parameters which can affect the results of the simulation. These parameters are generally related with the methodology adopted to solve the problem.

This chapter presents the parametric study performed to some of the simulation parameters like the mesh size, the penalty factor and the time step factor. This study allows to set the new simulations with the correct input parameters, avoiding the trial and error which can be time consuming.

6.1 Parametric study procedure

The first step in this kind of parametric study is to investigate which variables or parameters produce bigger changes in the final results. As explain earlier, these parameters are generally dependent on the method adopted to solve the problem. For this reason, one can decided which parameters will become the object of study.

The next step is to define the base input parameters for the simulations, including the ones that will be studied. Afterwards, simulations are run varying the parameter in study while keeping the others. Results are then compared allowing to know the influence of the parameter variation on the final results.

The base parameters and a simulation setup adopted in this parametric study is present in the next table:

Table 6.1: Base simulation setup adopted in the parametric study.

Parametric study base parameters		
Body model	Rigid body	
Velocity model	Constant	
Initial velocity	6.15	m/s
Deadrise	30	degrees
Mesh size	1.25	mm
Penalty factor, PFAC	0.01	–
Time step factor	0.9	–
Nº of coupling points	3	–
Simulation time	0.03	s

Once again, the materials adopted for the wedge structure are the ones presented in chapter 3, however, as the body is modeled rigid, the material choice is not important.

It´s also important to state that the energy results presented in this chapter are produced by a wedge with a section depth of 1000 millimeters (third dimension).

6.2 Solver precision

One input setting that can be very important is the solver precision, which can be single or double. Running the simulations using the double precision solver increases the simulation time by at least 25%. Some type of analyses are more sensitive to the numerical roundoffs occurring during the simulation. If a simulation only requires single precision, running it with double precision will not produce better results.

In this case, being an explicit simulation, it's expected that double precision solver is needed, although its necessary to confirm it. The next figure presents the results on the average pressure acting on the wedge with both solvers:

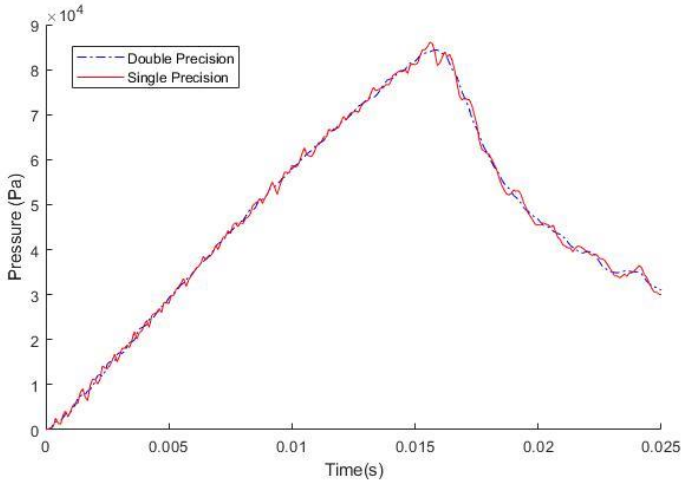

Figure 6.1: Average pressure comparison between single and double precision solvers.

Looking to the comparison figure one can conclude that the results are in good agreement, although the single precision solver produces a lot of oscillations when compared with the double precision one. For this reason, double precision will be used in all the other simulations of this study.

6.3 Penalty factor

As explained earlier, this ALE methods uses penalty forces to accomplish the coupling between the fluid and the structure. The penalty factor PFAC, is a scale parameter that acts on this penalty forces.

In the point view of the model accuracy it´s desirable that these penalty forces produce the smallest possible influence on the results, since they are used to model the fluid structure interface, but they don´t exist in reality. For this reason, it´s very important to fine tune the PFAC parameter.

LS-Dyna provides a specific output to quantify the energy absorbed by the coupling mechanism which is the contact energy output. The penalty factor should be tuned in a way that the contact energy absorbed at the coupling interface is small when compared to the internal energy, which is the energy contained in the system. In general, the smaller the contact energy result is, the better, has it means that the coupling mechanism is modeling the interface correctly without significant compromises in the results accuracy.

It´s possible for LS-Dyna to output a result with negative contact energy. This indicates that the model needs better parameter tuning and can also indicate other problems like leakage. This can be solved by decreasing the penalty scale factor, by decreasing the time step factor or by increasing the number of coupling points.

For PFAC parametric study, four values were chosen as indicated by the next input parameter table:

Table 6.2: Input parameters used for the PFAC parametric study.

PFAC study parameters		
Body model	Rigid body	
Velocity model	Constant	
Initial velocity	6.15	m/s
Deadrise	30	degrees
Mesh size	1.25	mm
Penalty factor, PFAC	0.5 / 0.1 / 0.01 / 0.001	–
Time step factor	0.9	–
Nº of coupling points	3	–
Simulation time	0.03	s

The results for the average pressure, internal energy and contact energy are present by the next set of figures:

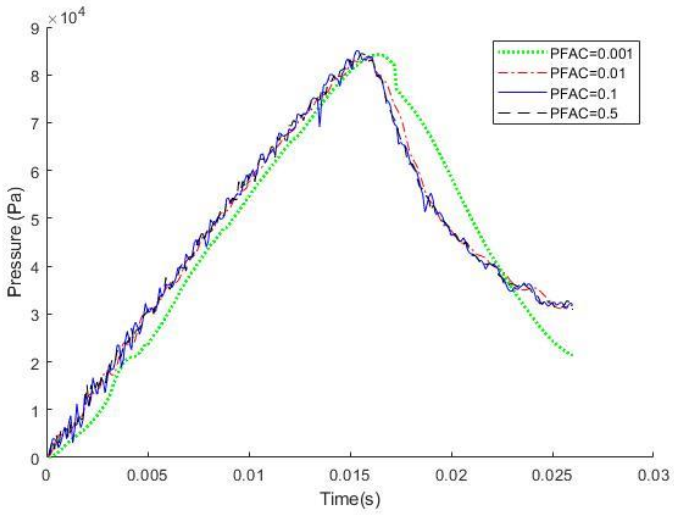

Figure 6.2: Average pressure comparison, PFAC parametric study.

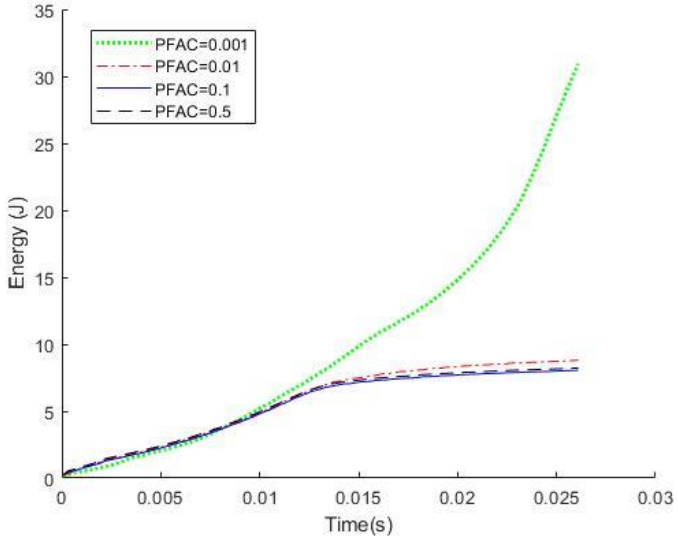

Figure 6.3: Global internal energy comparison, PFAC parametric study.

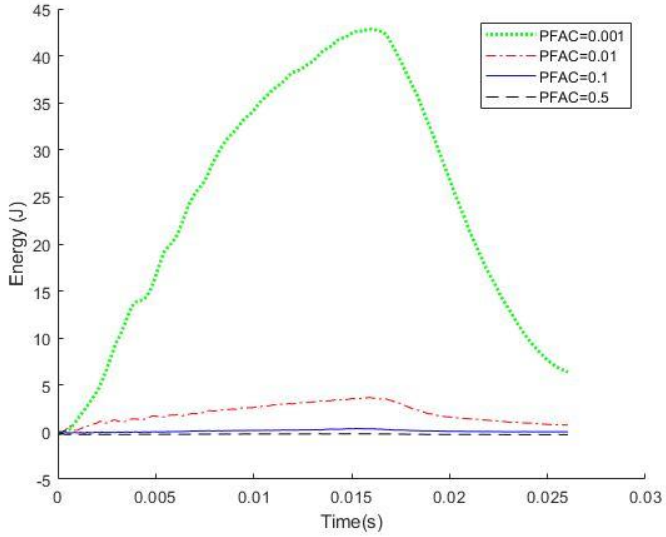

Figure 6.4: Contact energy comparison, PFAC parametric study.

The figures present the two extremes cases when setting the PFAC parameter. The lower value of PFAC shows that the coupling is too ‘rigid’, hence the reason for the contact energy to be very high when compared to the other values. This induces changes in the whole model, as can be seen by the difference in the average pressure and by the difference in the system internal energy.

On the other extreme, the higher PFAC value resulted in negative contact energy, which should be avoid for the reasons explained earlier. With PFAC set to 0.1, the contact energy is positive and very small in the first part of the simulation but then becomes negative, indicating that this value is near the optimum value for PFAC but still not adequate due to the negative contact energy.

For these reasons, 0.01 is the value adopted for the other simulations on this study, as the contact energy in those, is positive and is small when compared to the peak value of the system internal energy. The average pressure result for this PFAC value is slightly smoother than the others.

6.4 Time step factor

The time step factor it´s an input parameter in LS-Dyna which enables the user to establish a scale coefficient in relation to the critical time step calculated by the software, as explained earlier.

Generally, it´s safer to adopt a smaller time step than the critical time step, but this practice does not necessarily results in better numerical results. Reducing the time step factor can help solving instability issues but will also result in longer simulation times.

Three values for the time step factor were chosen for the parametric study as presented by Table 6.3:

Table 6.3: Input parameters used for the time step factor parametric study.

Time step factor study parameters		
Body model	Rigid body	
Velocity model	Constant	
Initial velocity	6.15	m/s
Deadrise	30	degrees
Mesh size	1.25	mm
Penalty factor, PFAC	0.01	–
Time step factor	0.4 / 0.6 / 0.9	–
Nº of coupling points	3	–
Simulation time	0.03	s

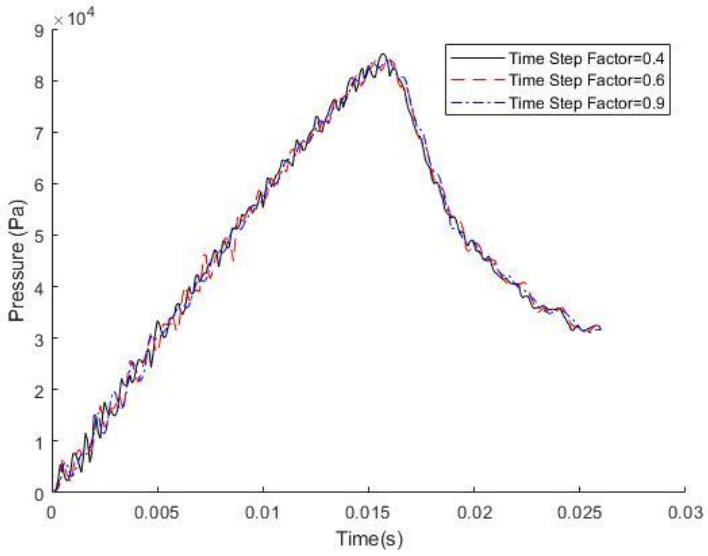

Figure 6.5: Average pressure comparison, time step factor parametric study.

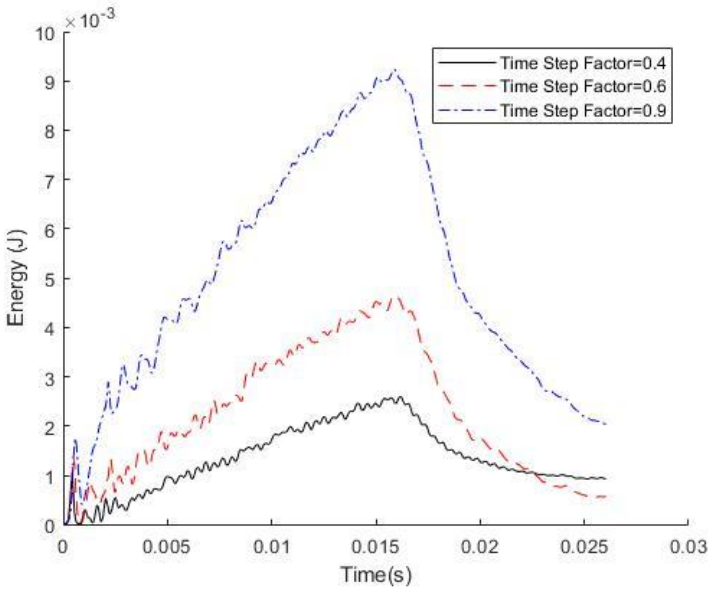

Figure 6.6: Contact energy comparison, time step factor parametric study.

The contact energy results presented by the Figure 6.6, show that reducing the time step factor will result in a smaller contact energy, which is desirable. On the other hand, the pressure results demonstrated by Figure 6.5 show that, in this case, the time step factor didn´t originated pressure results with relevant difference.

One should also notice that the contact energy results, although different from each other, are also very small when compared to the global energy. For this reason, the time step factor should be set to 0.9 to optimize the simulation time and only needs to be reduced is simulation instability is verified.

6.5 Mesh size

When studying any kind of fluid or structural problem using computational methods, the mesh size is usually one off the most important aspects of the model.

The classical approach to optimize this parameter is to start the simulation with a larger mesh and then start decreasing the element size while comparing the results obtained each mesh. Mesh size is one of the parameters that influence the most the computational time, being so important that it can even compromise the results applicability.

As suggested by Luo et al. [13], three mesh sizes were selected, as can be seen in the next table:

Table 6.4: Input parameters used for the mesh size parametric study.

Mesh size study parameters		
Body model	Rigid body	
Velocity model	Constant	
Initial velocity	6.15	m/s
Deadrise	30	degrees
Mesh size	5 / 2.5 / 1.25	mm
Penalty factor, PFAC	0.01	–
Time step factor	0.9	–
Nº of coupling points	3	–
Simulation time	0.03	s

Table 6.5 presents a general overview of different models used in this study. The grid refinement factor is a factor which relates the element size of each model. In this case, the mesh refinement factor is relating the wedge element number of each model.

The table also present the computing time and memory required for each simulation. The workstation used for this study is a 16-core machine at 3.4 GHz and is equipped with 32 GB of RAM.

Table 6.5: Mesh properties of the different models.

Parameter	***Model 1***	***Model 2***	***Model 3***
Element size	5mm	2.5mm	1.25mm
Nº of fluid elements	4725	14490	49500
Nº of structure elements	464	928	1856
Nº of elements in the FSI interface	58	116	232
Mesh refinement factor	4	2	1
Computing time (h:min)	0:04	0:19	1:17
Memory required (GB)	2.8	8.2	23.2

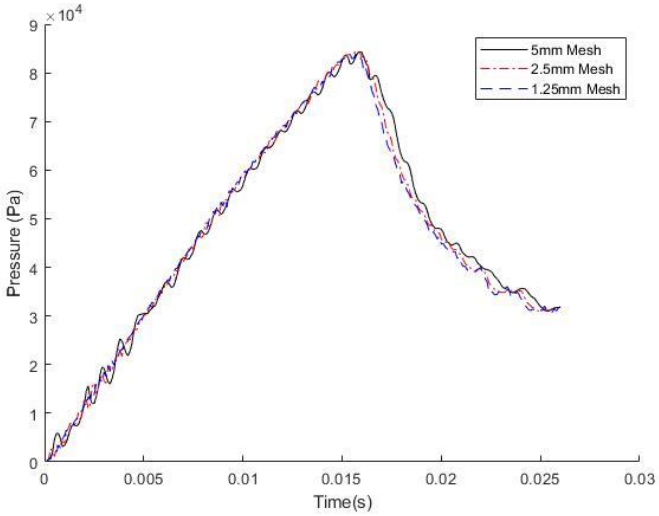

Figure 6.7: Average pressure comparison, mesh size parametric study.

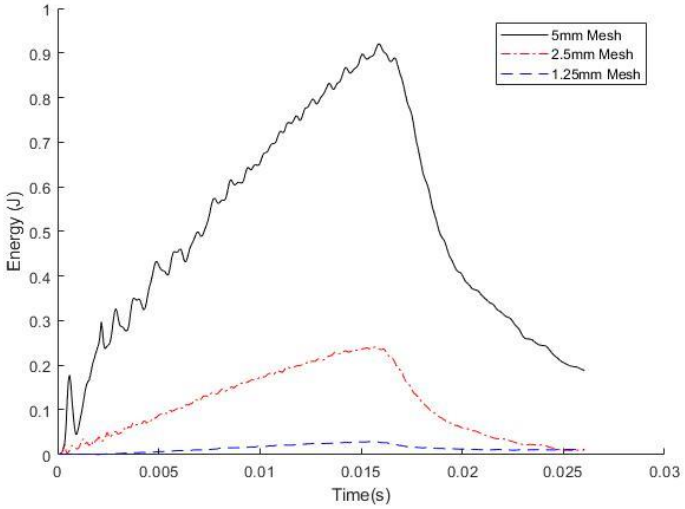

Figure 6.8: Contact energy comparison, mesh size parametric study.

The last figures demonstrate the results of the contact energy and the pressure for each mesh size. The pressure results indicate that all the models are in good agreement but it's also possible to notice that the smaller the mesh, the smother the results are. The contact energy results show that the small element mesh resulted in the smaller contact energy, which is desirable.

Another technique to study the mesh size is to produce a convergence result. In this case the result taken for the convergence analysis was the maximum value of the non-dimensional pressure coefficient.

Plotting the pressure coefficient results for each mesh size in respect to the mesh refinement factor and fitting a spline curve to the results it´s obtained the following figure:

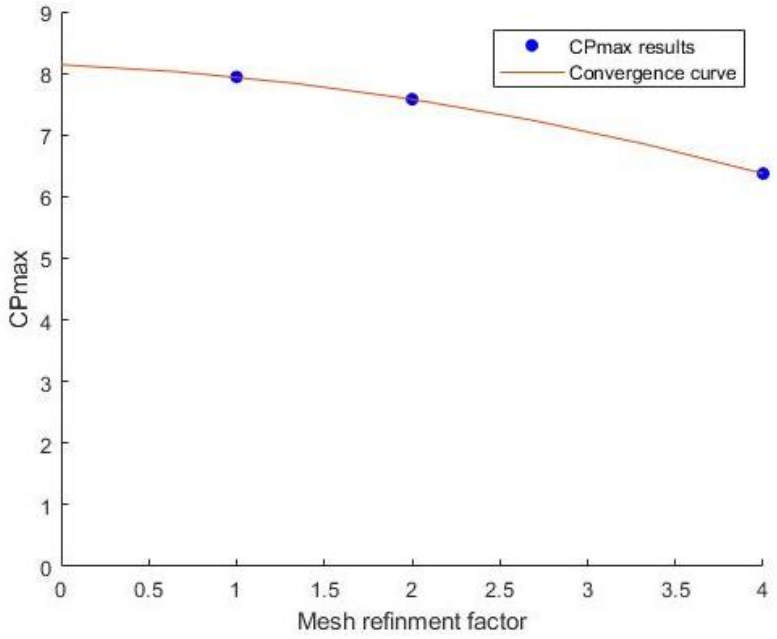

Figure 6.9: Maximum CP coefficient convergence.

The results presented by the last figure show that the value of the maximum non-dimensional pressure coefficient should converge to a value slightly higher than 8. The value obtained in the small element mesh (refinement factor equal to one) is already very close to this value. On the other hand, the value obtained with the 5mm element size model is near 20% lower, hence the importance of the mesh size.

6.6 Parametric study final discussion

The results showed that some parameters are more important than others when addressing the model configuration. As usual with this type of computational simulations, the mesh size is one of the most important settings. The finer mesh not only outputs smoother results but it´s also required to capture the peak values of the results. However, a compromise between simulation time and results accuracy should be made. In this case, given the processing power available for this study, the simulation with the finer mesh only took about 2 hours of simulation. For this reason, all the following simulations will be run with the 1.25mm element size mesh.

The penalty factor setting can impose some differences in the results, especially when set to the extreme values. Together with the time step factor, these input parameters should be set to in such way that the contact energy is the smallest without affecting too much the computational time.

The table 6.1 presented in the beginning of this chapters presents a set of input parameters that revealed to be a good starting point when setting new simulations.

This page was intentionally left blank

7. Hydroelasticity study

This chapters presents the study of the hydroelasticity effect during water impact through the comparison of the rigid body results with the flexible composite ones. Additionally, different simulations are run, varying the deadrise angle and the impact velocity. The results are then summarized and discussed.

7.1 Hydroelasticity model

The numerical model adopted for this study is similar to the ones presented earlier. The composite geometry, materials and boundary conditions are the ones presented in chapter three, only varying the deadrise and the impact velocity. Additionally, the section depth (third dimension) adopted to present dimensional results like the slamming forces and the energies is 500 mm.

Three cases of deadrise angle were chosen to be simulated in conjunction with four different velocities as presented in Table 7.1. The table also presents the other input parameters:

Table 7.1: Input parameters used for the hydroelasticity size parametric study.

Hydroelasticity study model parameters		
Body model	Rigid and Flexible	
Velocity model	Constant	
Initial velocity	4 / 6 / 8 / 10	m/s
Deadrise	10 / 20 / 30	degrees
Mesh size	1.25	mm
Penalty factor, PFAC	0.01	–
Time step factor	0.9	–
Nº of coupling points	Between 3 and 5	–

The simulation time is different for each simulation and can be calculated by the equation (3.7), resulting in the following:

Table 7.2: Hydroelasticity model simulation time in seconds

Deadrise / Velocity	***4 m/s***	***6 m/s***	***8 m/s***	***10 m/s***
10º	0.017	0.012	0.009	0.007
20º	0.030	0.019	0.015	0.012
30º	0.042	0.028	0.021	0.017

7.2 Rigid and composite body force comparison

The hydroelasticity effect study starts with the comparison of the results obtained for the rigid structure with the ones obtained for the flexible composite structure, for all the deadrise and velocity cases.

Figure 7.1 presents the results comparison, in which the slamming force time histories containing all the deadrise cases are presented for the each drop velocity case:

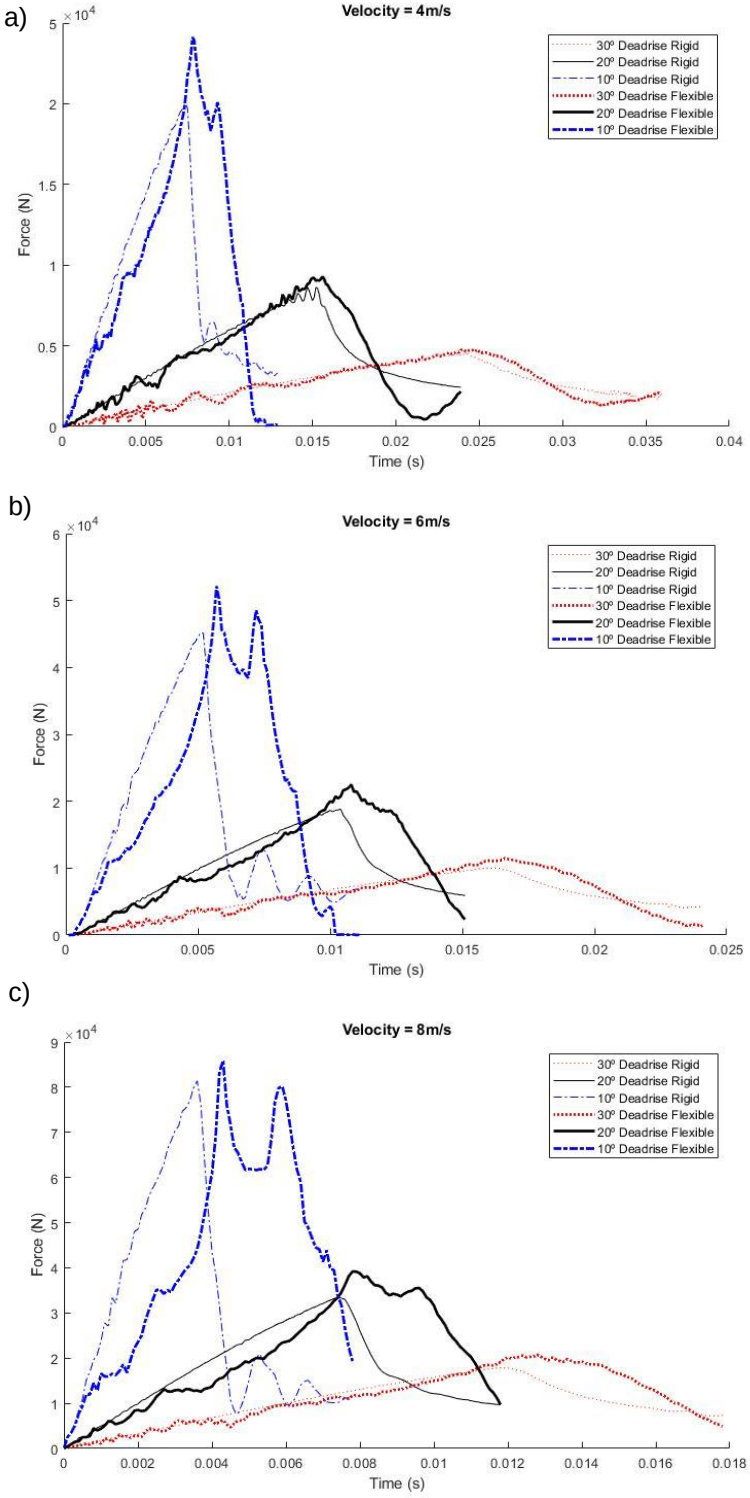

d)

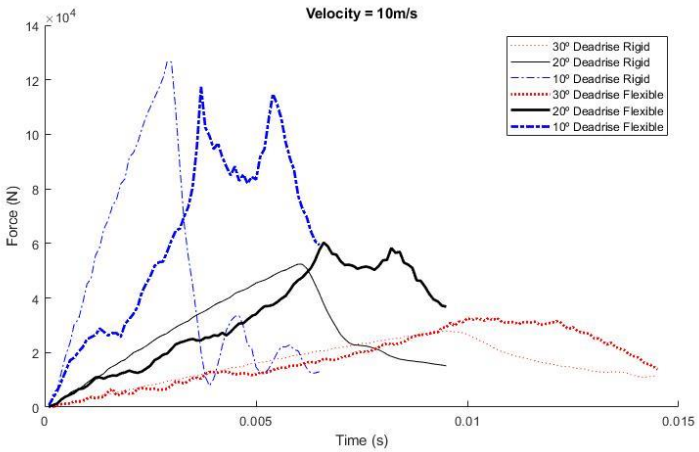

Figure 7.1: Rigid and flexible composite body´s slamming force comparison, fixed velocity. a) 4 m/s; b) 6 m/s; c) 8 m/s; and d) 10 m/s.

The results show that, in general and when referring to the low velocity 30º and 20º deadrise entries, the forces rise similarly in both the rigid and flexible composite cases, but the flexible body will present a higher force peak. This is to be expected due to the fact that, in the flexible body, the wedge structural displacement will result in a smaller local deadrise which then results in higher pressures.

The higher drop velocities will present very noticeable differences between the rigid and the flexible bodies. In the first stages of the impact, the force result observed in the flexible body is lower than rigid body but then, the flexible body present higher forces during a longer time. This effect is explained by the elastic behavior of the body, in which the impact is firstly dampened by the body elasticity, presenting its pressure value in a later stage of impact. At these deadrise and velocities combinations, the peak average force presented in the flexible case can be lower than the rigid one, although the energy absorbed in the flexible case is much larger than the in the rigid one, as will be demonstrated later.

When the local deadrise decreases significantly due to the extreme displacements in the wedge, the time history will present a double force peak. This effect is highly visible in the 10º deadrise cases. The first peak corresponds to the water reaching the wedge end while the seconds peak is due to the pressure accumulation below the wedge due to the extreme wedge deflection, as can be observed later in the pressure contours.

7.3 Pressure distribution comparison at given time instants

The non-dimensional pressure coefficient comparison between the rigid and flexible bodies for a given time instant will now be presented. The next first set of figures present an extended overview of the hydroelasticity effect for the 30º deadrise, 6 m/s case.

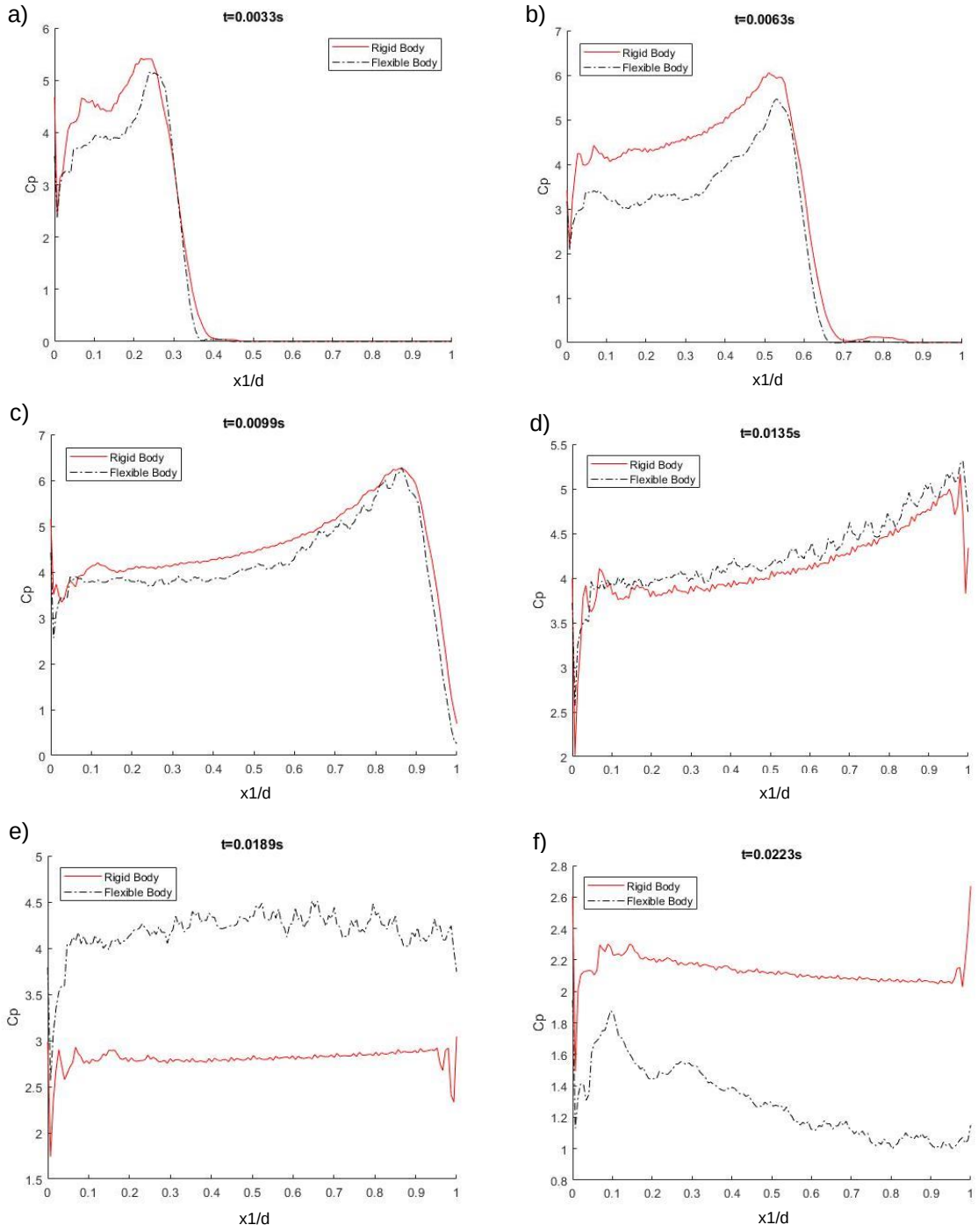

Figure 7.2: Rigid and flexible composite bodies pressure comparison at given time instants for the 30º deadrise, 6 m/s drop case. a) t=0.0033s; b) t=0.0063s; c) t=0.0099s; d) t=0.0135s; e) t=0.0189s; f) t=0.0223s.

The pressure distribution results presented in the previous figures are in good agreement with the results presented in Figure 7.1, for the average force results along the wedge with 30º deadrise with a drop velocity of 6m/s. Both results indicate that the pressure distribution is similar in both flexible composite and rigid bodies for the first stages of the drop tests, with the hydroelasticity effect occurring on the

flexible body presenting itself during the middle stage of the impact, before quickly dropping to a lower pressure value than the rigid body.

For the extreme case, 10º deadrise with a drop velocity of 10m/s, its obtained:

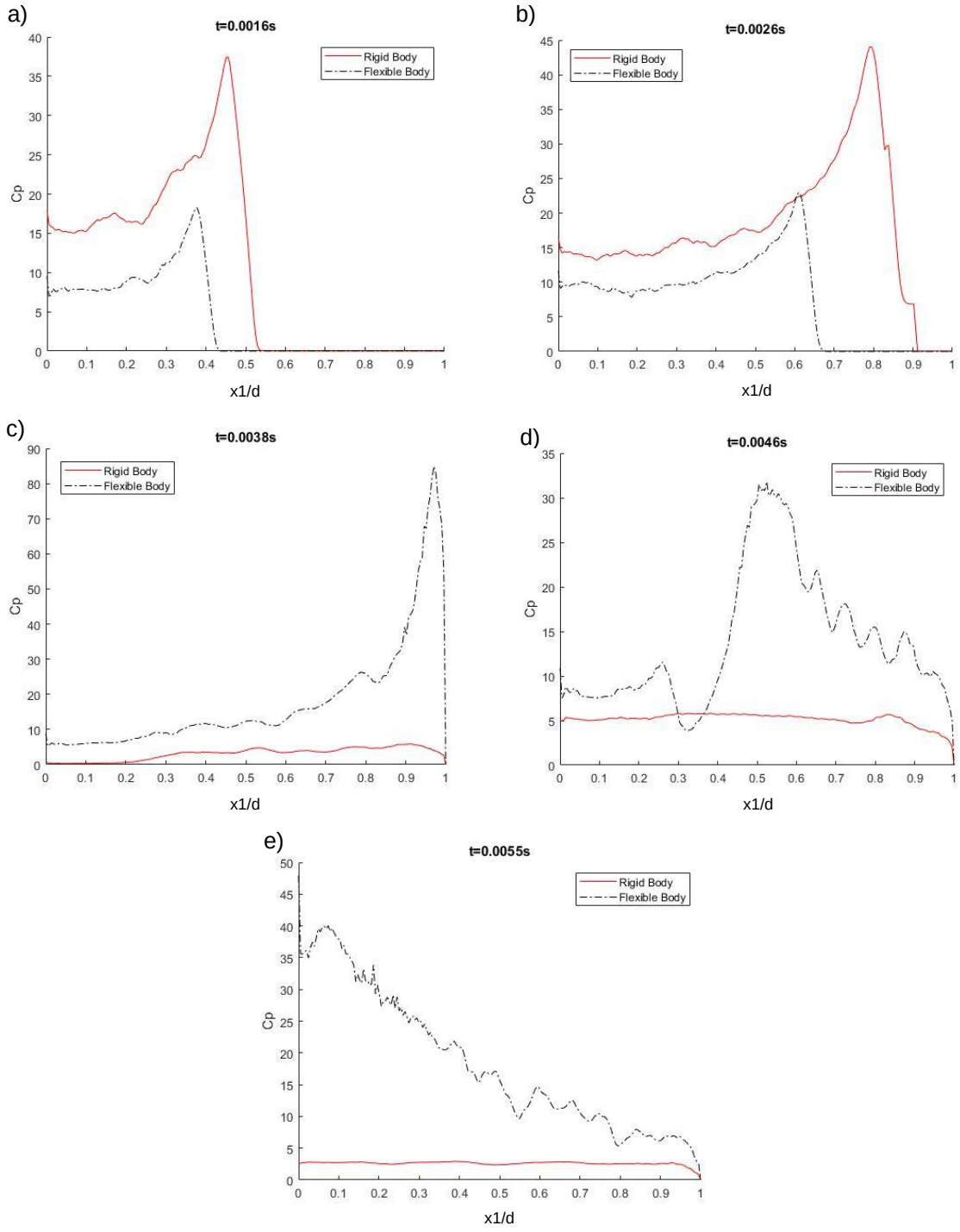

Figure 7.3: Rigid and flexible composite bodies pressure comparison at given time instants for the 10º deadrise, 10 m/s drop case. a) t=0.0016s; b) t=0.0026s; c) t=0.0038s; d) t=0.0046s; e) t=0.0055s.

Observing the pressure distribution results above, the comparison of the first time instants, t=0.0016s and t=0.0026s, indicate that in both cases the maximum pressure location is moving towards the wedge end, with the rigid case demonstrating higher pressure, which is consistent with the average force results presented earlier. As explained earlier, this effect can be explained by the elastic body behavior which dampens the impact due to its elasticity. The time instant t=0.0038s corresponds to the instant were the water jet reaches the end of the wedge in the elastic case, and this also corresponds to the first slamming force peak observed in the average slamming forces results presented earlier. In comparison, the pressure in the rigid case had already decreased. The extreme structural deflection in this case, will result in pressure accumulation below the wedge, and for this reason the higher pressures will hold longer before dropping to lower values as is the case with the rigid body. The maximum pressure location will then travel backwards towards the wedge keel, as demonstrated by the time instants figures, t=0.0046s and t=0.0055s.

7.4 Pressure distribution comparison at given locations

In similarity with the results presented earlier, the non-dimensional pressure coefficient comparison is now presented for the locations proposed earlier in this study. These results are once again presented for the 30º deadrise, 6 m/s case:

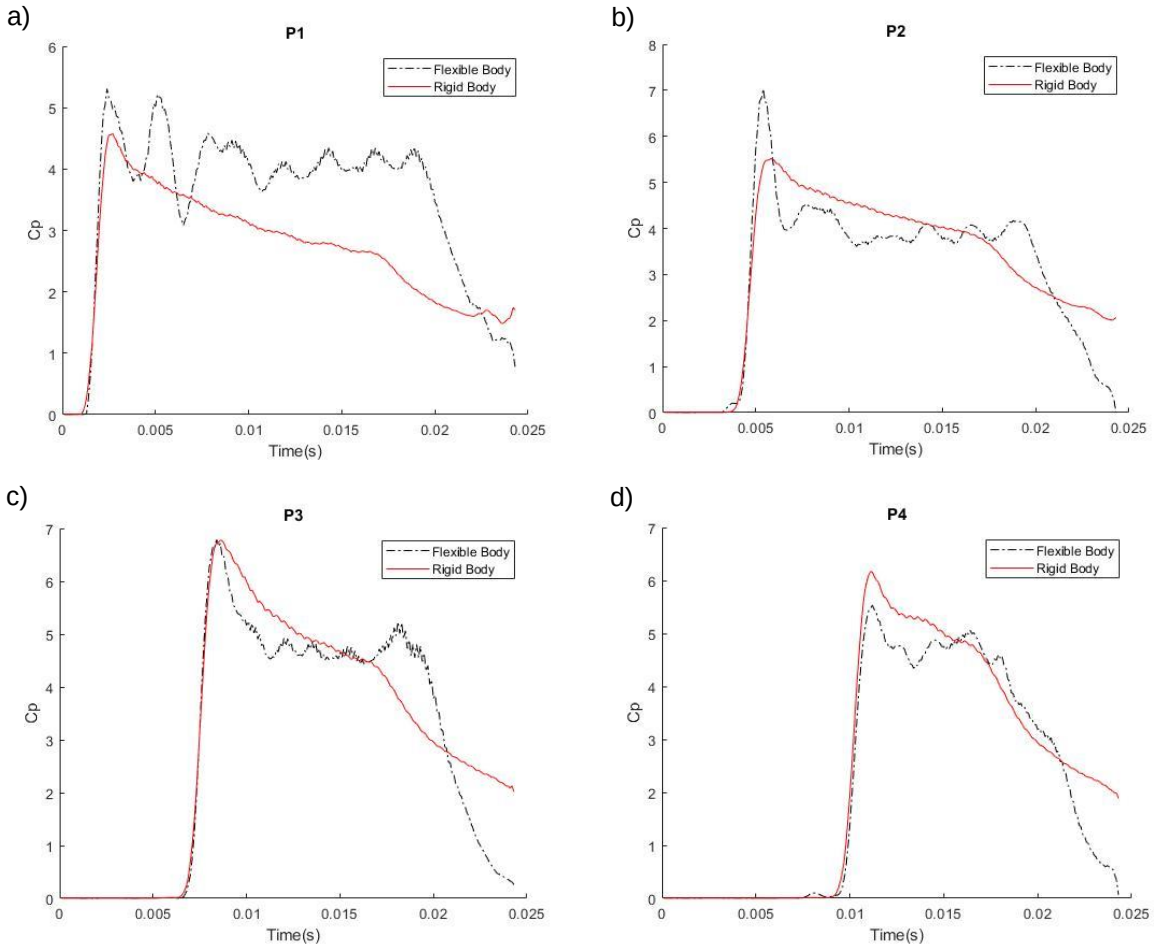

e)

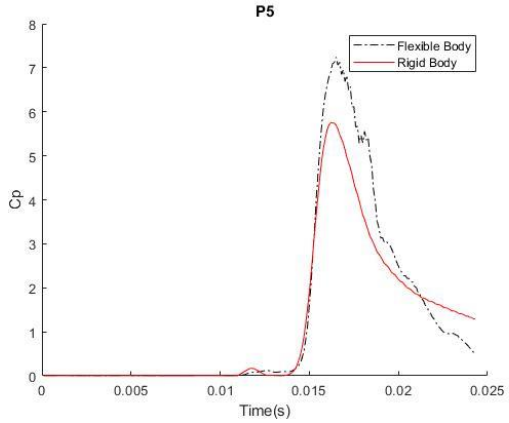

Figure 7.4: Rigid and flexible composite bodies pressure comparison at given locations for the 30º deadrise, 6 m/s drop case. a) P1; b) P2; c) P3; d) P4; e) P5.

The results presented in Figure 7.4, show that, near the end of the wedge, the pressures acting on the flexible composite case are higher than the rigid ones. Between point P2 and P4 which corresponds to the region between one fourth and three fourths of the wedge length, the pressure is similar in both rigid and flexible cases. In the keel zone, the pressures acting on the flexible composite body are higher than for the rigid case.

Figure 7.5 presents the pressure distribution for the 10º deadrise, 10m/s case:

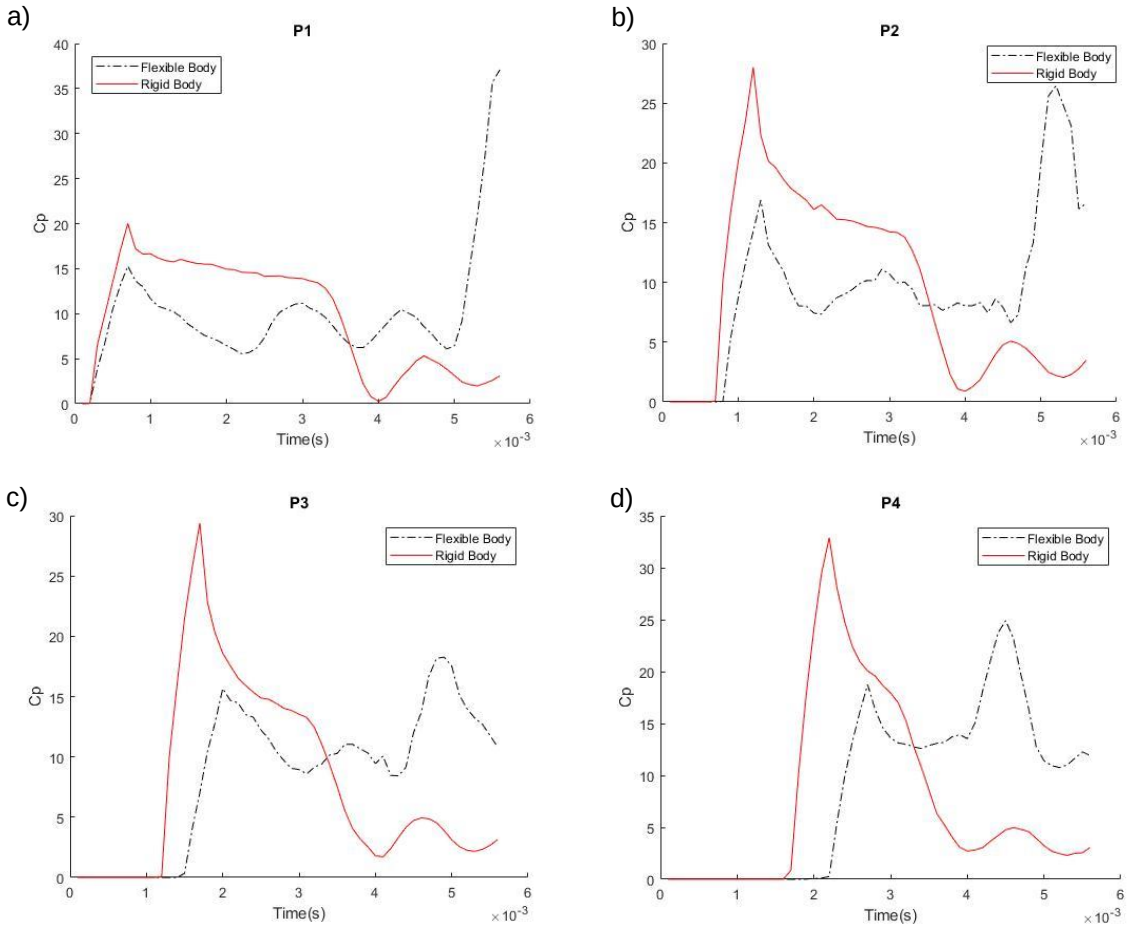

e)

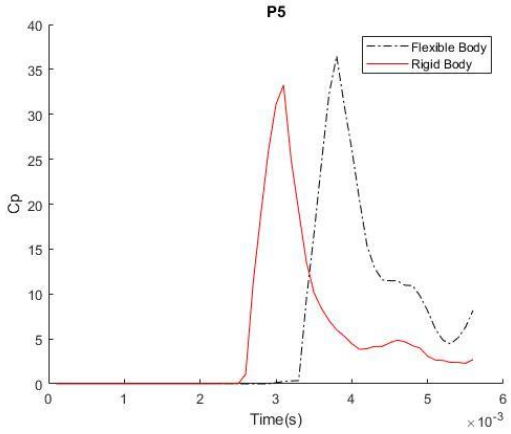

Figure 7.5: Rigid and flexible composite bodies pressure comparison at given locations for the 10º deadrise, 10 m/s drop case. a) P1; b) P2; c) P3; d) P4; e) P5.

The pressure distribution comparison for given locations corroborate the explanations presented earlier. The double pressure peak present in the flexible cases in the P1 to P4 locations correspond to the pressure increase towards the wedge end during the water entry, which quickly drops when the water reaches the wedge end, as can be seen in the P5, which is near the wedge end. Afterwards, the pressure starts to increase again towards the wedge keel, hence the double peak effect that can be observed here and also in the average slamming forces figures. The difference in the initial recording of the pressure between the flexible and rigid case is due to structural displacement in the flexible case. This effect was not present in the 30º deadrise 6m/s drop velocity case because the structural displacement is much lower, as will be presented later.

7.5 Rigid and flexible composite body energy comparison

After presenting the pressure comparison of the elastic and rigid bodies, it's also interesting to perform the same comparison in the energy point of view. The following figures show the comparison of the evolution of the internal energy present in the system (structure and fluid):

a)

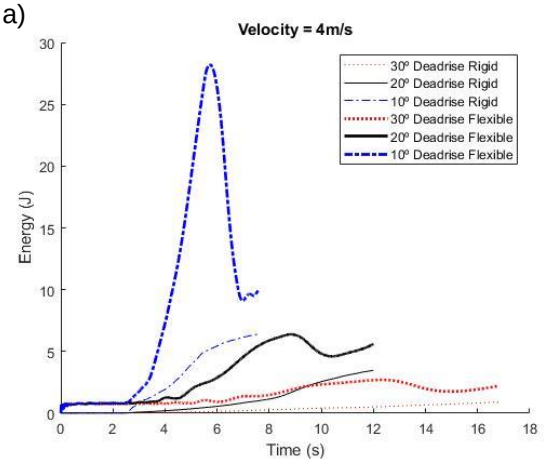

b)

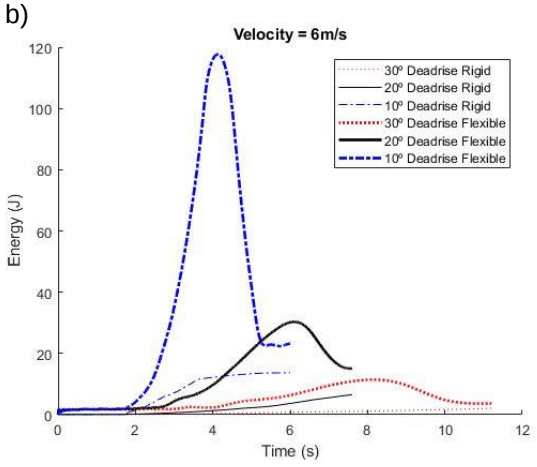

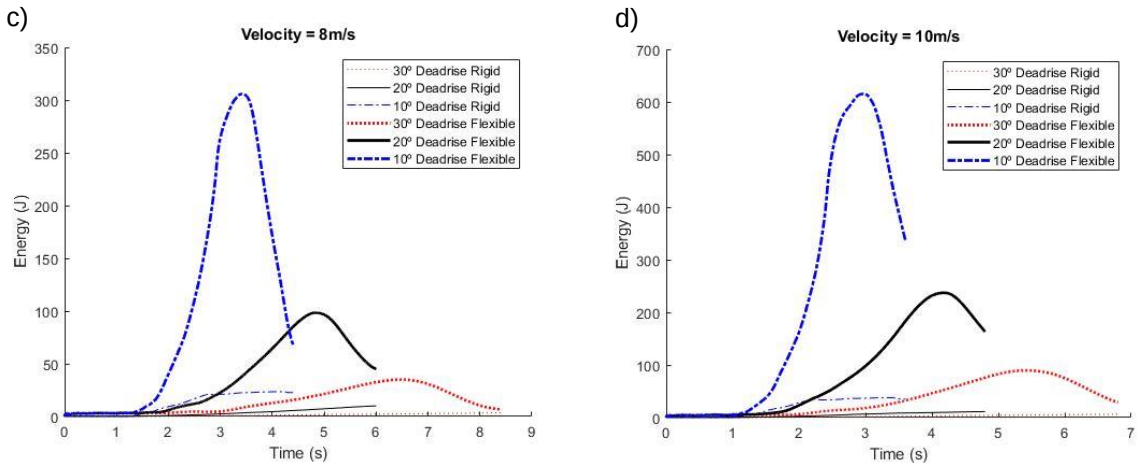

Figure 7.6: Water entry internal energy comparison, fixed velocity. a) 4 m/s; b) 6 m/s; c) 8 m/s; and d) 10 m/s.

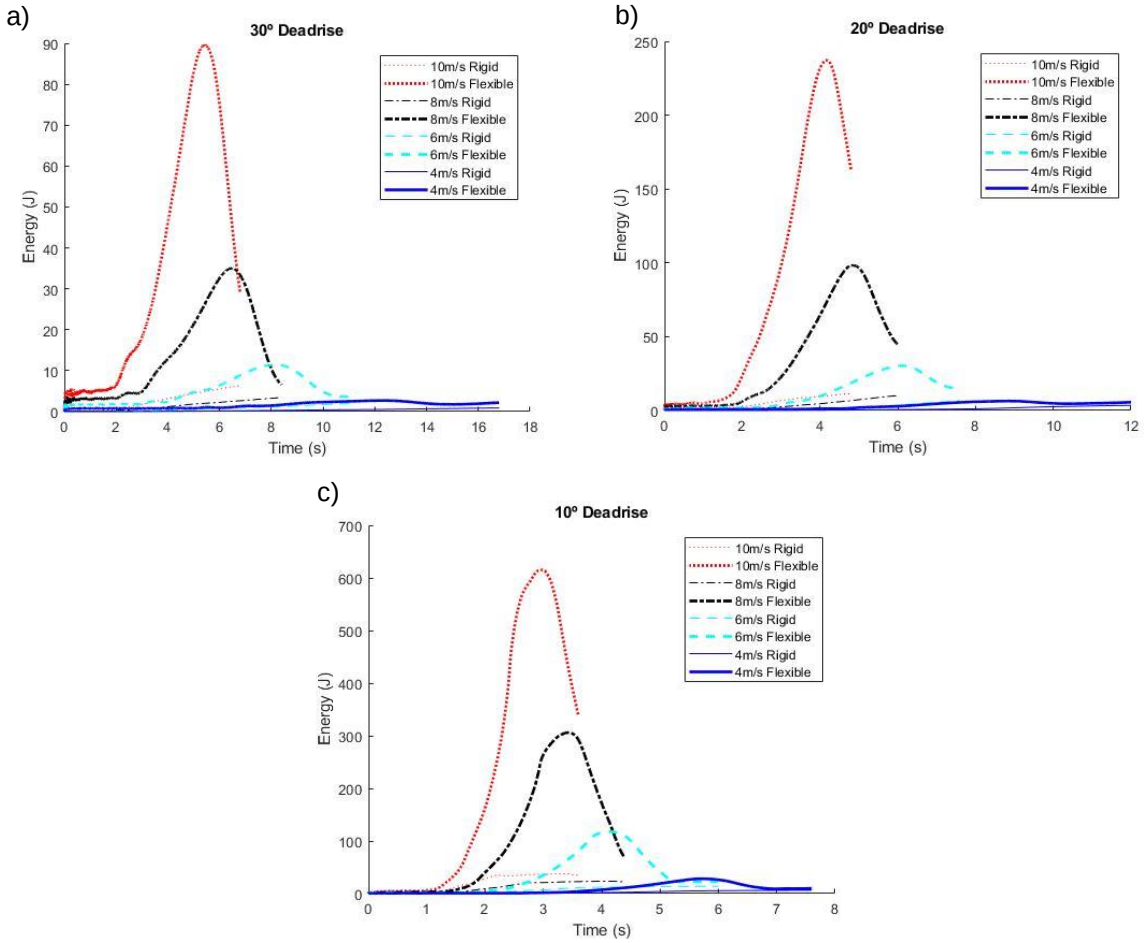

Figure 7.7: Water entry internal energy comparison, fixed deadrise. a) 30º; b) 20º; c); 20º.

Figure 7.6 presents a general overview of the energy results for all the deadrise cases and with a fixed drop velocity, in both the rigid and flexible composite cases. On the other hand, Figure 7.7 presents similar content but with the combination of the velocities.

The figures show a big difference between the rigid case and the flexible composite one, indicating that hydroelasticity is a very relevant aspect when dealing with slamming impacts. It's also clear that the internal energy increases very fast when the deadrise decreases. It´s important to clarify that this is the total internal energy, which includes the fluid and the structure bodies. In the case of the rigid body simulation, as the structure is rigid, its internal energy is zero, hence, the small energy observed in the rigid body cases.

The behavior of the energy curves is in good agreement with the pressure curves presented earlier, meaning that the pressure increase during the water entry will result in the structure displacement which translates in the increase of the internal energy. When the pressure drops due to the flow separation, the structure will start to return to its original shape, decreasing the displacement and the internal energy.

7.6 Flexible body slamming force

After comparing the results between the flexible composite and the rigid wedge, the study proceeds with the comparison of other variables, like the flexible wedge slamming force, between the different combinations of deadrises and velocities.

Firstly, the results with fixed velocity for the different deadrises are presented and then the results with fixed deadrise:

a)

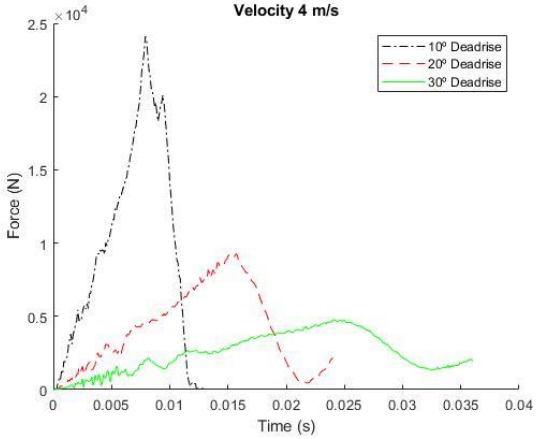

b)

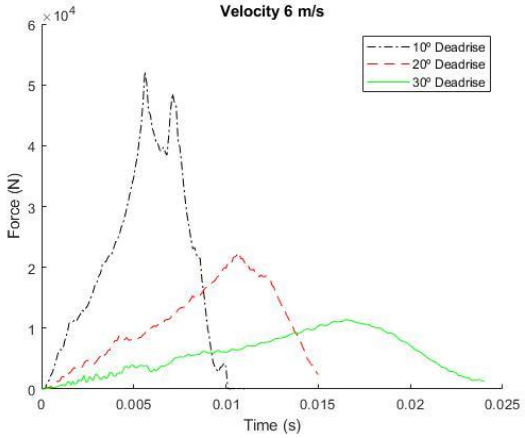

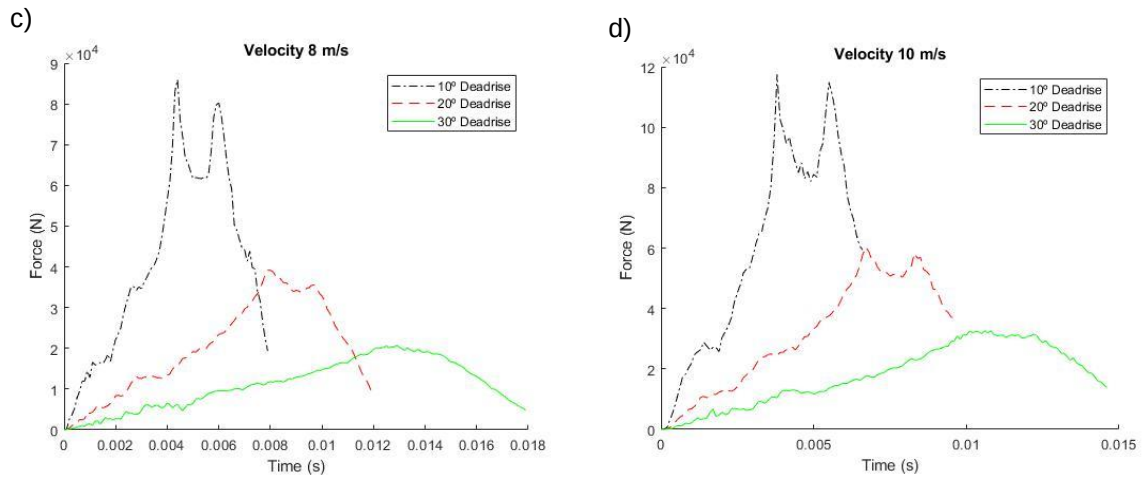

Figure 7.8: Flexible composite body slamming force comparison, fixed velocity. a) 4 m/s; b) 6 m/s; c) 8 m/s; d) 10m/s.

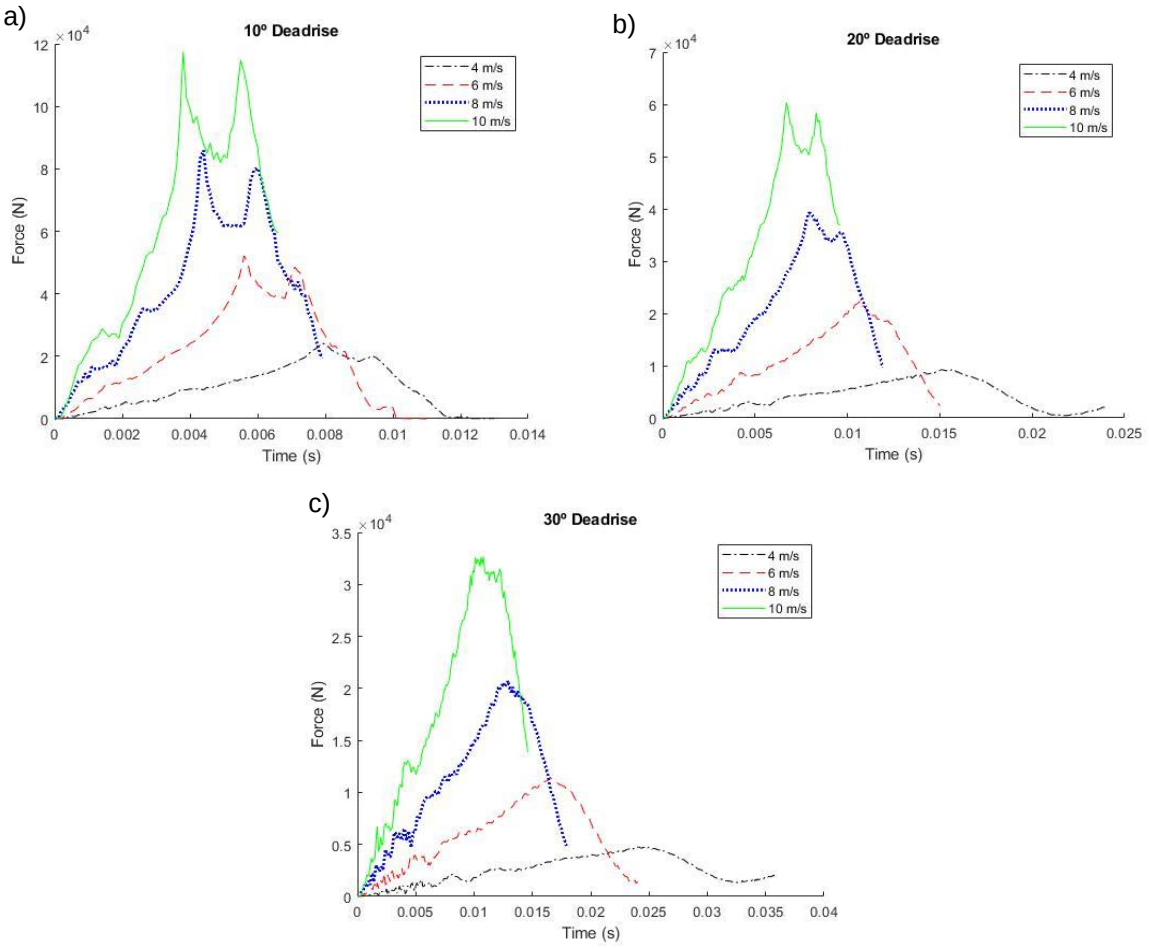

Figure 7.9: Flexible composite body slamming force comparison, fixed deadrise. a) 10º; b) 20º; c) 30º.

The slamming force curves presented above show good agreement with each other. As expected, the higher deadrise and lower drop velocities result in lower forces and smoother force time history curves.

The second peak effect, which was explained earlier, is also present here in all the 10º deadrise results. The peak effect is larger when the velocity is higher, which seems right, since the higher velocity will also result in higher structural displacement which is related to the peak effect. This effect can also be observed, at a smaller scale, in the 20º deadrise case but only when the drop velocity is high.

7.7 Displacement at middle point comparison

This study also includes the evaluation of the flexible composite body displacement along the water entry. The displacement at the middle point of the wedge is taken between the wedge current position along the simulation and an imaginary line that connects the keel point and the chine. This line corresponds to the *x1* axis of the local coordinate system presented in chapter 3, Figure 3.7.

The results are presented in the same way as the ones presented before, first by presenting the results with fixed velocities:

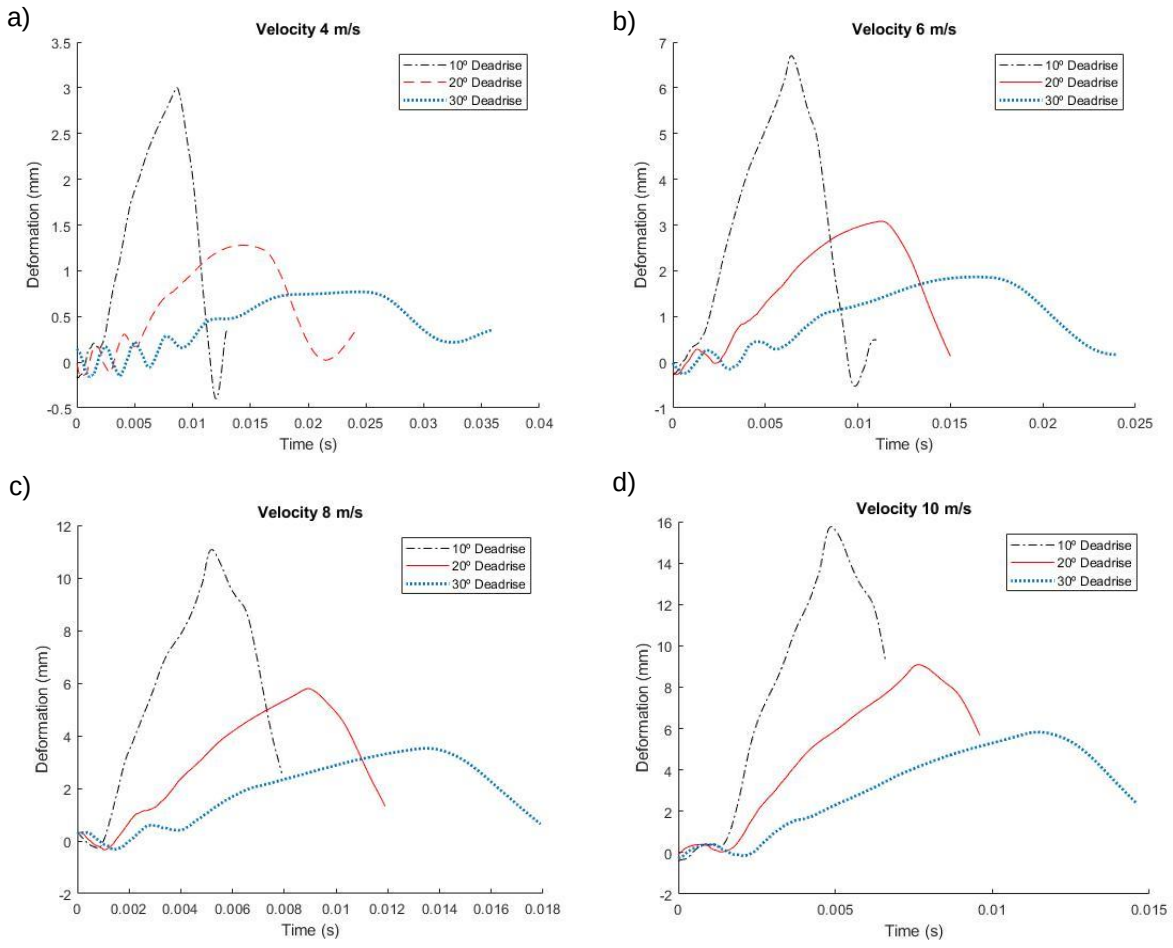

Figure 7.10: Flexible composite body middle point displacement comparison, fixed velocity. a) 4 m/s; b) 6 m/s; c) 8 m/s; d) 10 m/s.

Followed by the results presented with fixed deadrise:

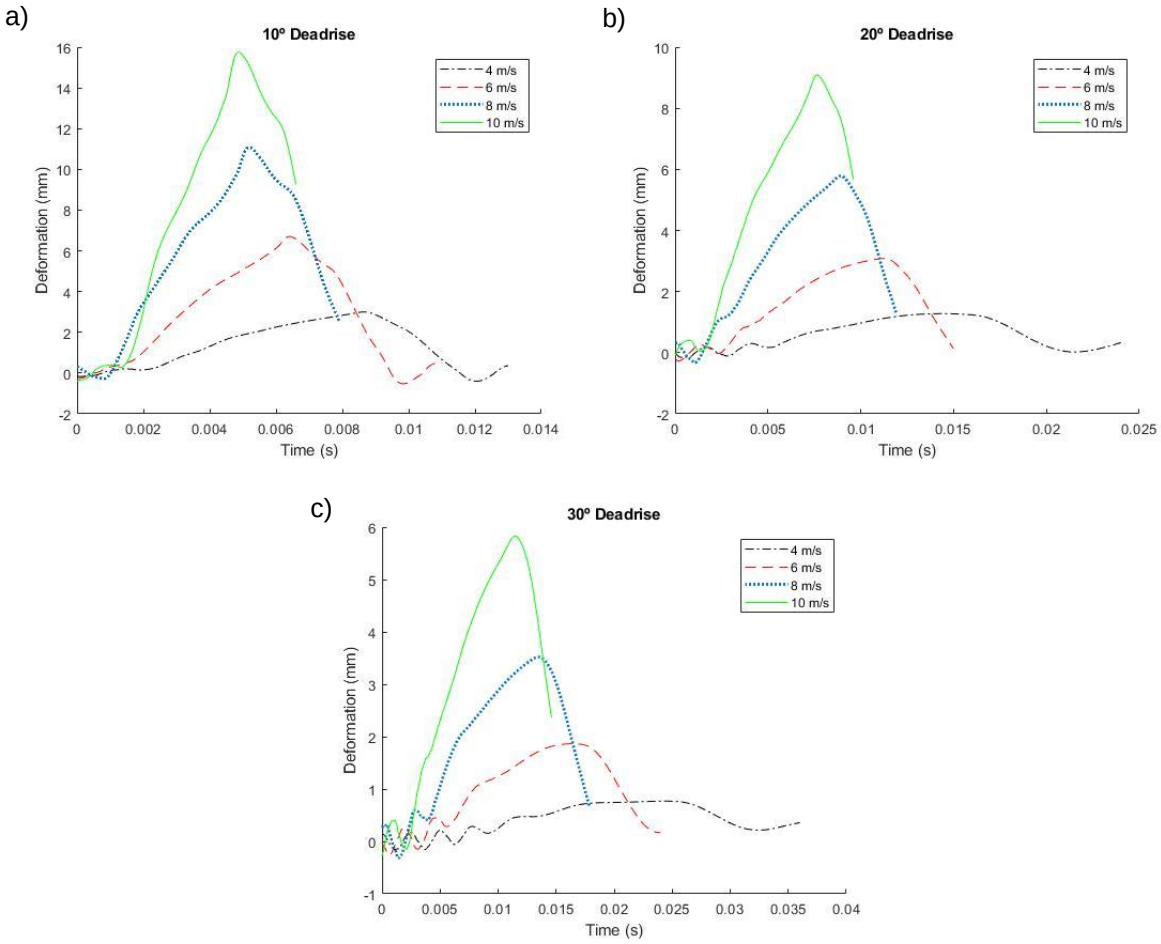

Figure 7.11: Flexible composite body middle point displacement comparison, fixed deadrise. a) 10º; b) 20º; c) 30º.

The results show good agreement which each other, since the differences between the results when the drop velocity or the deadrise changes are consistent.

One can notice that the slower and higher deadrise experiments show prolongated initial stages of vibration. This is somewhat expected, since that in these cases, the structure inertial forces are still relevant when compared to the slamming forces, which is not the case when considering high drop velocity's and low deadrises.

The second peak effect observed and explained earlier can, once again, be observed in the 10º deadrise displacement curves, as the rate of descent after the peak value of these curves is not constant as in the other cases.

7.8 Free surface and pressure contours overview

The free surface and pressure contours are now presented for the different deadrise cases at 6 m/s drop velocity. Starting by the 30º deadrise:

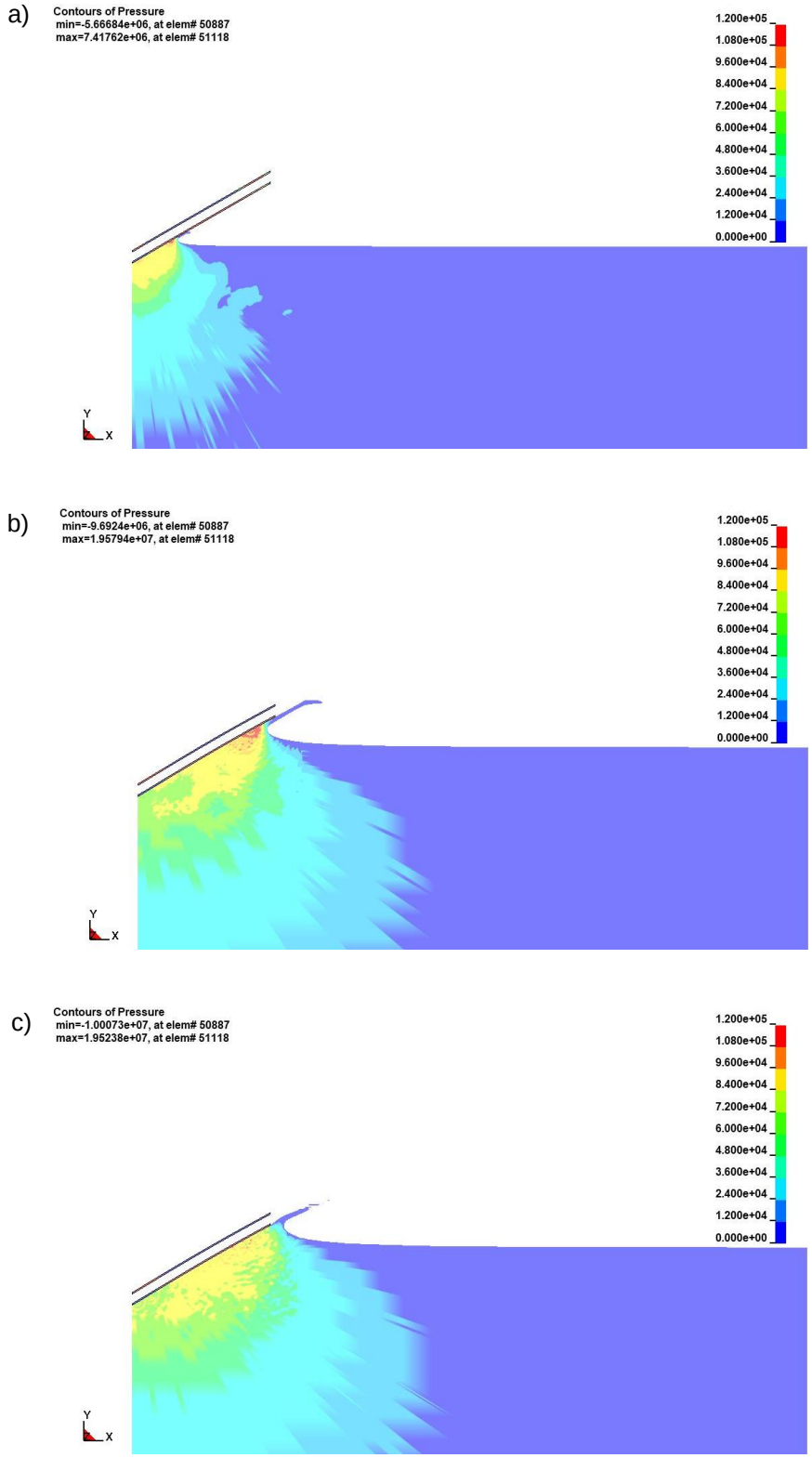

Figure 7.12: Water entry of the flexible composite wedge with 30º deadrise, 6 m/s drop velocity. a) Initial stage; b) Before flow separation; c) After flow separation.

Looking the past figures one can clearly identify the pressure drop after the flow separation. As this is the flexible composite wedge, structural bending also starts to be noticeable, especially in the later stages of the water entry. The 20º deadrise case is presented next:

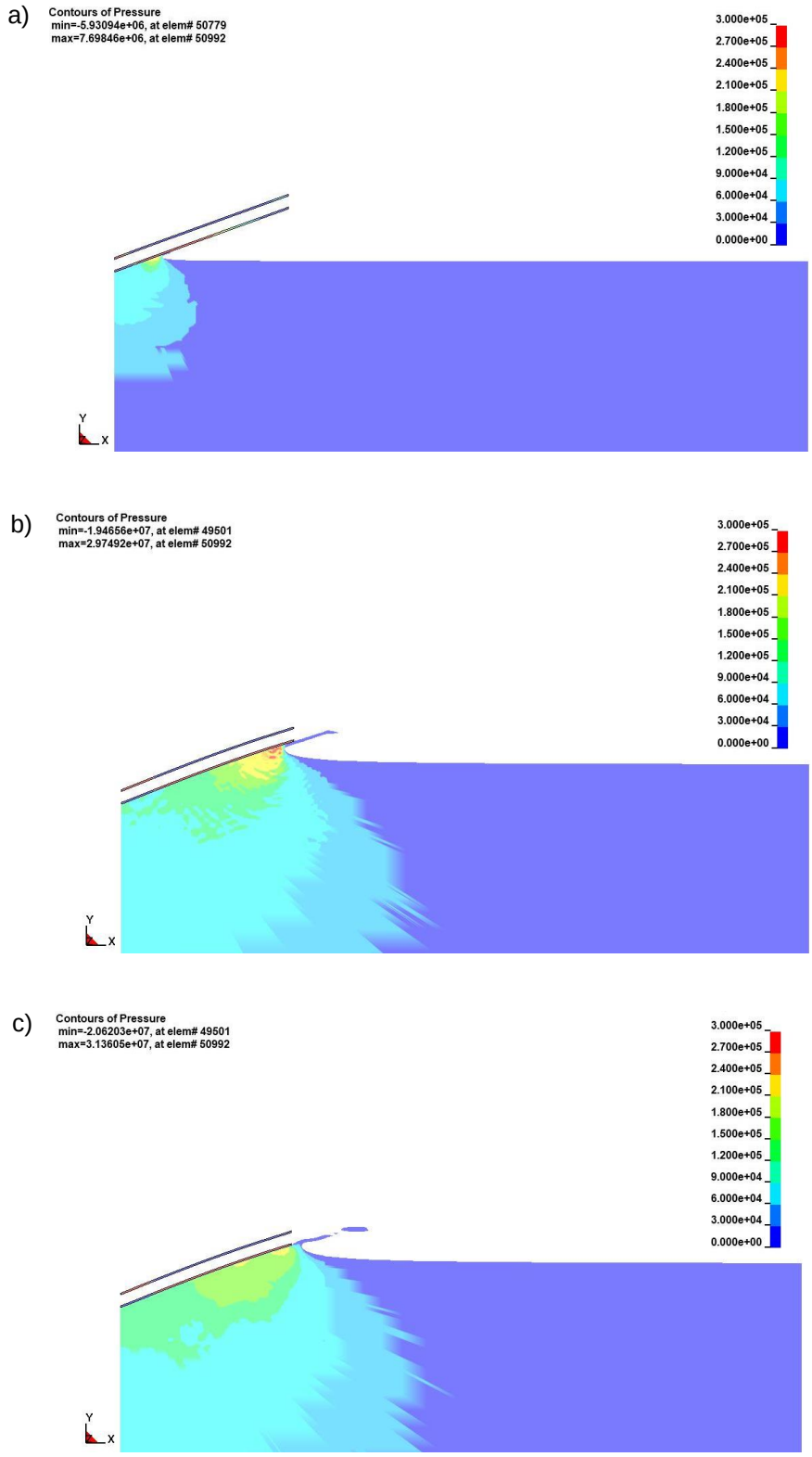

Figure 7.13: Water entry of the flexible composite wedge with 20º deadrise, 6 m/s drop velocity. a) Initial stage; b) Before flow separation; c) After flow separation.

With a smaller deadrise, the pressure rises as expected and the bending suffered by the structure is even higher:

Finally, the 10º deadrise case is presented:

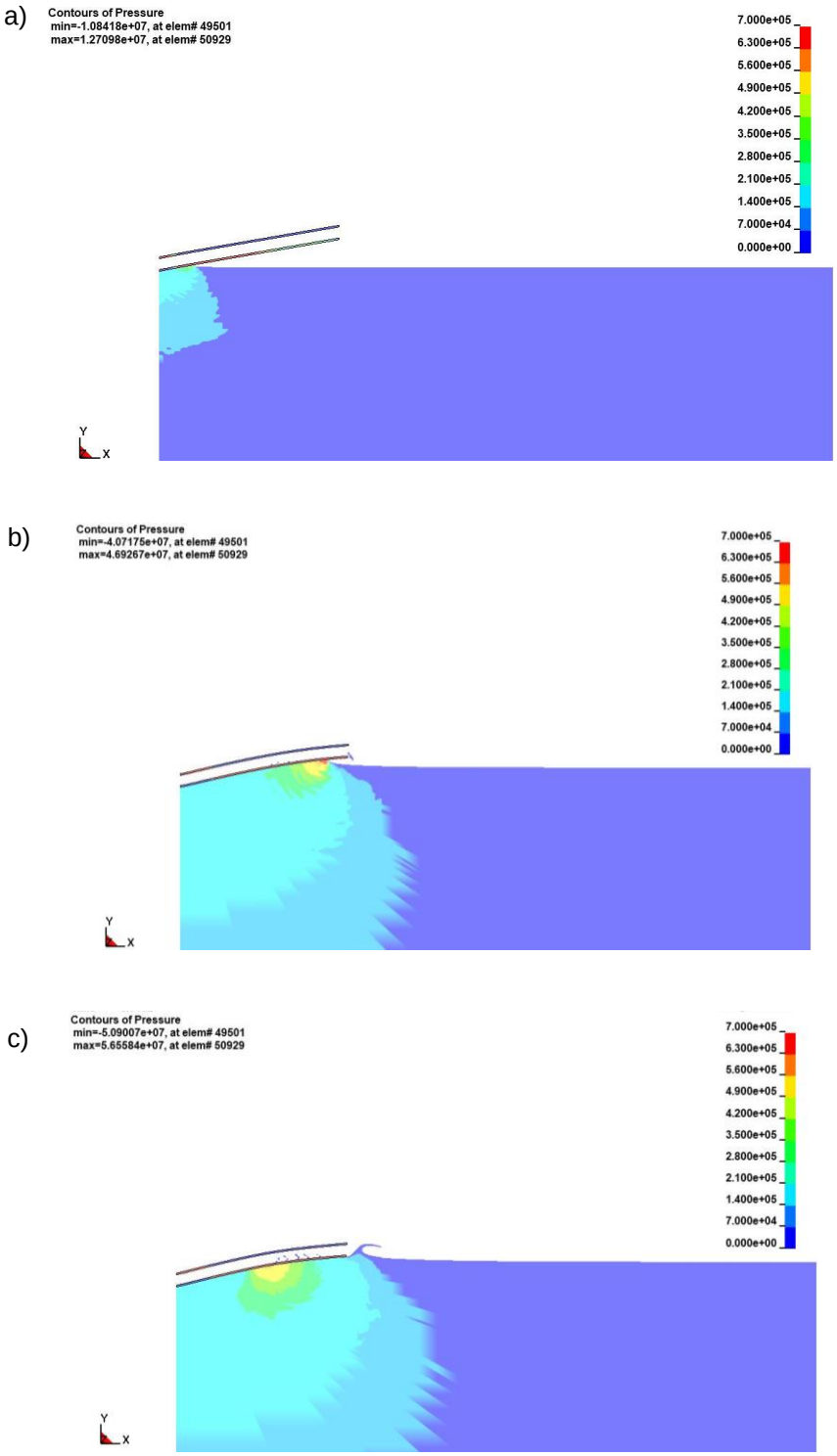

Figure 7.14: Water entry of the flexible composite wedge with 10º deadrise, 6 m/s drop. a) Initial stage; b) Before flow separation; c) After flow separation.

The previous figure presents the water entry of the composite wedge with a deadrise of 10º. This case presents an additional effect due to the extreme deadrise and structural displacement. As the displacement is so high, when the water entry is near its final stage, the local deadrise is smaller than 10º. Being the deadrise so close to zero, the pressure buildup below the wedge is very high, as can be seen in the Figure 7.15.

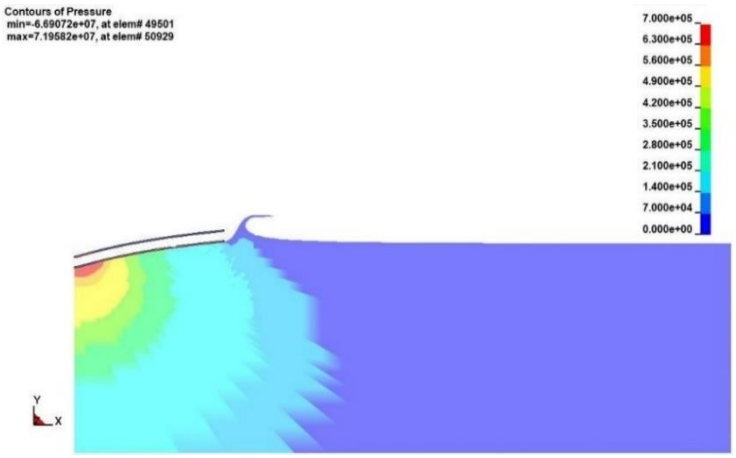

Figure 7.15: Pressure build up below the wedge, 10º deadrise, 6 m/s drop.

This is the effect that presented itself in a form of a double peak in the force time histories of the Figures 7.8 and 7.9.

7.9 Hydroelasticity study final discussion

The hydroelasticity study to the water entry of a composite wedge was performed combining different values of deadrise and drop velocity. The rigid body forces and energy results for the all the deadrise and velocity combinations were also compared with the flexible composite body ones.

Overall, the results show good agreement with each other as the time histories obtained for the energies, forces and displacements are similar and present the same effects.

The rigid and flexible composite body comparison results also indicate that the hydroelasticity can play an important role on the overall pressure results, especially when the displacement on the structure is high which is the case of high speed and low deadrise water entries.

Finally, and in an additional note, the displacements observed in the high velocity, low deadrise cases were very high, which indicate that, if damage was considered, the structure could have already been suffering of problems like delamination. Although this type of analysis is out of the scope of this study, verifications should be performed. In this case, the most relevant stresses that should be analyzed when working with sandwich composite structures are the maximum tensile and compressive stresses at the skins and the shear stress occurring at the core.

This page was intentionally left blank

8. Conclusions

8.1 Final remarks

The water entry of two-dimensional composite wedges was simulated using the LS-Dyna commercial code which is equipped with an Arbitrary Lagrangian Eulerian (ALE) solver. The penalty method was the coupling algorithm adopted to model the fluid structure interface.

The composite structure was fully modeled in solid elements, which is advantageous if the user is interested in the out of plane stress/strain results. This required the composite material properties in the out of plane direction, which were obtained from the Bureau Veritas rules for the classification of composite vessels. These properties are a good guideline for the design of structures with composites, however, since the composite materials are very sensitive, one should not take them for granted. Proper material testing must always be performed.

The simulation with the 30º deadrise angle rigid wedge, free drop case, was carried in order to validate the model. The comparison with the other available numerical, experimental and analytical indicated good agreement between the results. Small differences on the pressure peak value was noted when comparing the computational results with the experimental results proposed by Zhao et al. [27] which are slightly smaller. One of the possible causes for this difference in the peak value of the pressure is due to the fact the computational formulation is modeled as an infinite length three-dimensional wedge which is not the case of the model used in the experiments. Hence, it's possible that the experiments resulted in smaller values due to the pressure losses at the boundary of the wedge.

On the other hand, the simulation of the 10º deadrise angle flexible composite wedge, modeled according to Hassoon et al. [10] research, also indicated good results correlation. Once again, small differences were observed in the peak values of the slamming forces but the difference in dimensionality is also present, meaning that the results difference can be caused by the same reasons stated in the rigid body case. Other experimental errors are a possibility since the experimental results were also slightly different from the numerical results presented on the same research.

When using computational tools like LS-Dyna, it´s very important that the user fully understand the mechanics and theories behind the software, as this will ease the parameter tuning process. The parametric study presented earlier show, once more, that the mesh is one of the most important setting, since a better mesh should produce smoother results and offer better peak value capture. It´s important to state that a better mesh does not necessarily means a smaller mesh, since that with smarter mesh refinements it's possible to obtain better results with less processing time. In the case of this specific software and method, other parameters like the penalty factor or the time step factor may have to be adjusted during the tuning process, hence the importance to fully understand the method and its limitations.

Finally, the comparison between the flexible composite and the rigid wedge proved that the hydroelasticity is an effect that must certainty induce additional loads on the structure, especially when the structure has a low stiffness, since the bigger the displacement the higher are the additional pressure loads caused by the hydroelasticity effect.

As the main objective for this thesis was to investigate the effects of the slamming problem when considering a composite structure, it´s possible to make two major conclusions regarding the subject. One, is the fact that this method as proved to be reliable enough to perform the analysis of the water entry, and, second, is the fact that the hydroelasticity effect can, certainly, be very problematic for a composite build vessel.

8.2 Future works

Suggestions for extending this work can include the study of stress distribution along the wedge and for the different deadrise and velocities cases.

It could also be interesting to extend this work by implementing a damage model that would consider the delamination at the core-skin interface and the other failure types, which enables to understand how the damage occurs and propagates with these types of loadings and structures.

Other possible study is the one that considers hybrid laminates or other fiber types for the composite structure. For instance, combining glass fibres with carbon fibres in the laminate can prove to be viable as the carbon high modulus, should substantially reduce the hydroelasticity effect, reducing the forces and stresses on the structure. The price difference between these materials, can be compensated by the fact that the option with higher modulus is more expensive but will require less material. This by itself could be addressed by an economic viability study.

Bibliography

[1] Alexandru, I., Brizzolara, S., Viviani, M., Couty, N., Donner, R., Hermundstad, O., Kukkanen, T., Malenica, S., and Termarel, P. (2007). Comparison of experimental and numerical impact loads on ship-like sections. *Advancements in Marine Structures, pp. 339-349.*

[2] Allen, T. and Battley, M. (2015). Quantification of hydroelasticity in water impacts of flexible composite hull panels. *Ocean Engineering. Vol. 100, pp 117-125*.

[3] Aquelet, N., Souli, M. and Olovsson, L. (2006). Euler-Lagrange coupling with damping effects: Application to slamming problems. *Computer Methods in Applied Mechanics and Engineering. Vol. 195, pp. 110-132*

[4] Armand, J.L. and Cointe, R. (1987). Hydrodynamic impact analysis of a cylinder. Proceedings of Fifth International Offshore Mechanics and Arctic Engineering Symp., Vol. 1, pp. 609-634.

[5] Bureau Veritas (2012). Hull in Composite Materials and Plywood, Material Approval, Design Principles, Construction and Survey. *NR 546 DT R00 E.*

[6] Cheng, H., Chao, F. (2011). Simulation of fluid-solid interaction on water ditching of an airplane by ALE method. *Journal of Hydrodynamics, Ser. B. Vol. 23, pp. 637-642.*

[7] Emami, Sadra (2017). Development of Probabilistic Models for Long Term Reliability of Sandwich Composites in Saline Freeze/Thaw Environment for Civil Engineering Applications.

[8] Faltinsen, O.M. (1999). Water entry of a wedge by hydroelastic orthotropic plate theory. *Journal of Ship Research. Vol.3, pp 180-193.*

[9] Hassoon, O.H., Tarfaoui, M., El Malk Alaoui, A. (2017). An experimental investigation on dynamic response of composite panels subjected to hydroelastic impact loading at constant velocities. *Engineering Structures. Vol. 153, pp 180-190.*

[10] Hassoon, O.H., Tarfaoui, M., El Malk Alaoui, A., El Moumen, A. (2017). Experimental and numerical investigation on the dynamic response of sandwich composite panels under hydrodynamic slamming loads. *Composite Structures. Vol. 178, pp 297-307.*

[11] Kaushik, D. and Batra, R.C. (2010). Local water slamming impact on sandwich composite hulls. *Journal of Fluids and Structures. Vol. 27, pp 523-551.*

[12] Lu, C.H., He, Y.S., Wu, G.X. (2000). Coupled analysis of nonlinear interaction between fluid and structure during impact. *Journal of Fluid and Structures. Vol. 14, pp. 127-146.*

[13] Luo, H., Wang, S., Guedes Soares, C. (2011). Numerical prediction of slamming loads on a rigid wedge subjected to water entry using an explicit finite element method. *Advances in Marine Structures, pp. 41-48.*

[14] Mei, X.M., Liu, Y.M. and Dick, K.P. (1999). On the water impact of general two-dimensional sections. *Applied Ocean Research. Vol. 21, pp. 1-15.*

[15] Ochi, M.K. and Motter, L.E. (1973). Prediction of slamming characteristics and hull response for ship design, *Transactions SNAME. Vol. 81, pp. 144-190.*

[16] Qin, Z. and Batra. R.C. (2008). Local slamming impact of sandwich composite hulls. *International Journals of Solids and Structures. Vol. 46, pp. 2011-2035.*

[17] Ray, M.C. and Batra, R.C. (2012). Transient hydroelastic analysis of sandwich beams subjected to slamming in water. *Thin-Walled Structures. Vol. 72, pp. 206-216.*

[18] Stavovy, A.B. and Chuang, S.L. (1976). Analytical determination of slamming pressures for high speed vessels in waves, *Journal of Ship Research. Vol. 20, pp. 190-198.*

[19] Stenius, I., Rosn, A. and Kuttenkeuler, J. (2006). Explicit Fe-modeling of fluid-structure interaction in hull-water impacts. *International Shipbuilding Progress. Vol. 53, pp. 1031-121.*

[20] Stenius, I., Rosn, A. and Kuttenkeuler, J. (2007). Explicit FE-modeling of hydroelasticity in panel-water impacts. *International Shipbuilding Prog. Vol. 54, pp. 111-127.*

[21] von Kármàn, T. (1929). The impact on seaplane floats during landing. *Technical Report, National Advisory Committee for Aeronautics.*

[22] Wagner, H. (1932) Uber Stossund Gleitvergange an der Oberflache von Flussigkeiten. *Zeitschrift fuer Angewandte Mathematik und Mechanik. Vol. 12, pp. 193–215.*

[23] Wang, S. and Guedes Soares, C. (2012). Analysis of the water impact of symmetric wedges with a multimaterial eulerian formulation. *International Journal of Maritime Engineering. Vol. 154, pp. 191-206.*

[24] Wang, S. and Guedes Soares, C. (2014). Slam induced loads on a bow-flare section with various angles. *International Journal of Maritime Engineering. Vol 156, pp. 303-314.*

[25] Wang, S. and Guedes Soares, C. (2014). Numerical study on hydroelastic water entry of a wedge. *Developments in Maritime Transportation and Exploitation of Sea Resources, pp 199-208.*

[26] Zhao, R. and Faltinsen, O.M. (1993). Water entry of two-dimensional bodies. *Journal of Fluid Mechanics. Vol. 246, pp. 593-612*

[27] Zhao, R., Faltinsen, O.M. and Aarsnes, J.V. (1996). Water entry of arbitrary two-dimensional sections with and without flow separation. *Proceedings of the 21st Symposium on Naval Hydrodynamics.pp. 408-423*

Appendix A – Material calculator

Composite Materials Properties, Bureau Veritas NR 546 DT R00 E

Materials Considerated		
Resin	Vinylester	
Reinforcement	E-Glass Woven Roving	
Weight Reeinf.	800	g/m^2
Process	Infusion	

Materials Propierties			
Resin			
rho_r	1.100	g/cm^3	Density resin
poisson_r	0.260	-	Poisson coefficient
E_r	3550	Mpa	Young Modulus
sigma_r	75	Mpa	Resin breaking stress
G_r	1400	Mpa	Shear Modulus
shearSig_r	65	Mpa	Shear breaking stress
CoefRes	0.90	-	
Fibers			
rho_f	2.570	g/cm^3	Density fiber
poisson_f0	0.238	-	Poisson coefficient at 0º
E_f0	73100	Mpa	Young Modulus at 0º
sigma_f0_ten	2750	Mpa	Tens. breaking stress at 0º
sigma_f0_comp	1750	Mpa	Comp. breaking stress at 0º
G_f	30000	Mpa	Shear Modulus
shearSig_f	1700	Mpa	Shear breaking stress
poisson_f90	0.238	-	Poisson coefficient at 90º
E_f90	73100	Mpa	Young Modulus at 90º
sigma_f90	1750	Mpa	Breaking stress at 90º

Laminate Properties			
Volume and mass fractions			
Vf	0.391	-	Fiber volume fraction
Vr	0.609	-	Resin volume fraction
Mf	0.600	-	Fiber mass fraction
Mr	0.400	-	Resin mass fraction
Laminate Thickness			
e_m	0.796	mm	Laminate Thickness
e_f	0.796	mm	
Laminate Density			
pho	1.675	g/cm^3	Laminate Density
Laminate Weight			
pho	1333	g/m^2	Laminate Density
Elastic Coefficients			
Cud1	1.00	-	
Cud2	0.80	-	
Cud12	0.90	-	
Cudp	0.90	-	

Unidirectional Laminate		
Elastic Properties		
E1	30744	Mpa
E2	6164	Mpa
E3	6164	Mpa
G12	2654	Mpa
G13	2654	Mpa
G23	1858	Mpa
n	0.911	-
v12	0.226	-
v13	0.226	-
v21	0.045	-
v31	0.045	-
v23	0.226	-
v32	0.226	-
poisson_f'	0.238	-
Breaking Stresses		
et1	2.70	-
et2	0.42	-
ec1	1.80	-
ec2	1.55	-
e12	1.80	-
e13,eIL2	1.80	-
e23,eIL1	2.50	-
sigma_t1	747	Mpa
sigma_t2	23	Mpa
sigma_c1	498	Mpa
sigma_c2	86	Mpa
sigma_12	43	Mpa
sigma_IL2,13	43	Mpa
simga_IL1,23	42	Mpa

Woven Roving Laminate		
Elastic Properties		
Ceq	0.500	-
Q11	31063	Mpa
Q22	6228	Mpa
Q12	1409	Mpa
Q33	2654	Mpa
A11	14844	N/mm
A22	14844	N/mm
A12	1122	N/mm
A33	2113	N/mm
E1	18539	Mpa
E2	18539	Mpa
E3	6164	Mpa
G12	2654	Mpa
G13	2388	Mpa
G23	2388	Mpa
v12	0.076	-
v13	0.226	-
v21	0.076	-
v31	0.136	-
v32	0.136	-
Breaking Stresses		
et1	1.80	-
et2	1.80	-
ec1	1.80	-
ec2	1.80	-
e12	1.50	-
e13,eIL2	1.80	-
e23,eIL1	1.80	-
sigma_t1	300	Mpa
sigma_t2	300	Mpa
sigma_c1	300	Mpa
sigma_c2	300	Mpa
sigma_12	36	Mpa
sigma_IL2,13	39	Mpa
simga_IL1,23	39	Mpa

Choped Strand Mat Laminate		
Elastic Properties		
E1	15381	Mpa
E2	15381	Mpa
E3	6164	Mpa
G12	5916	Mpa
G13	1858	Mpa
G23	1858	Mpa
v12	0.300	-
Breaking Strains and Stresses		
et1	1.55	-
et2	1.55	-
ec1	1.55	-
ec2	1.55	-
e12	2.00	-
e13,eIL2	2.15	-
e23,eIL1	2.15	-
sigma_t1	215	Mpa
sigma_t2	215	Mpa
sigma_c1	215	Mpa
sigma_c2	215	Mpa
sigma_12	106	Mpa
sigma_IL2,13	36	Mpa
simga_IL1,23	36	Mpa